**Title** Generative mechanisms and scaling laws of EEG suggest an alternative physiological interpretation of ICA

**Author line** Komal K. Kukkar[1], Hyeonseok Kim[2], Pranav J. Parikh[1], Makoto Miyakoshi[2,3]

**Author affiliations**

1. *Center for Neuromotor and Biomechanics Research, Department of Health and Human Performance, University of Houston, Houston, TX 77004-6015*
2. *Division of Child and Adolescent Psychiatry, Cincinnati Children's Hospital Medical Center, Cincinnati, OH 45229*
3. *Department of Psychiatry and Behavioral Neuroscience, University of Cincinnati College of Medicine, Cincinnati, OH 45219-0559*

**Corresponding author** Makoto Miyakoshi (ORCID 0000-0002-4062-6679)

**Preprint servers** (n.a.)

**Classification** Biological Sciences, Biophysics and Computational Biology.

**Keywords** EEG, independent component analysis (ICA), dipolarity

**Abstract**

In this study, we subject the conventional physiological interpretation of independent component analysis (ICA) applied to EEG, the small-patch model, to systematic falsification, and propose an alternative large-patch model. The small-patch model assumes that ICs correspond to localized cortical patches with < 1 cm². However, this assumption has remained unvalidated. The small-patch model predicts that approximately 70% of sources are localized within sulci up to 15 mm deep, with rapidly changing dipole orientations across the cortex. In contrast, the large-patch model (>6–10 cm²) predicts relatively stable radial orientations accompanied by physiologically implausible source depths due to depth bias. First, we conducted a stimulation study using a forward–inverse modeling framework with a four-layer head conductor model. We confirmed that depth bias emerges when a single equivalent dipole is fitted to a potential field generated by a broad array of parallel dipoles. This observation led to the key hypothesis that the presence of depth bias in empirical data would favor the large-patch model. Second, we analyzed resting-state EEG from two European open datasets comprising 820 recordings (62–64 channels), yielding dipole depth and orientation distributions for nearly 15,000 qualified brain ICs. Results showed that more than 80% of ICs were localized at physiologically implausible depths (19–26 mm), favoring the large-patch model. A novel dipole-orientation analysis revealed broad, low-spatial-frequency structure in dipole orientations, further supporting the large-patch model. We conclude that the revised physiological interpretation of ICA aligns with electrophysiological literature and computational insights into EEG-specific spatial scaling laws.

**Significance statement**

Independent component analysis (ICA) has been proposed as a promising tool for computational neuroscience using human scalp EEG. One of the original proponents introduced a physiological model suggesting that anatomically accurate neural sources could be directly recovered by applying ICA to EEG data. However, we found that this model assumes EEG generation within cortical patches smaller than 1 $cm^2$, which has remained unvalidated for over a decade and requires revision. Using both simulation and empirical EEG datasets, we demonstrated that our alternative model, involving larger cortical patches (>6–10 $cm^2$), better fits the electrophysiological generative model of scalp EEG signals. We conclude that our large-patch model provides an updated, more physiologically plausible interpretation of ICA results.

## Introduction

Independent component analysis (ICA) [1–3] has been widely used for preprocessing scalp-recorded EEG. Although its dominant application has been artifact rejection in sensor space [4–11], a pioneering group has used ICA to extract putative brain signals and reconstruct their temporal dynamics in an ICA-defined source space using clustering algorithms [12–22]. A central premise of this line of work is that brain ICs are physiologically valid because their scalp projections are highly dipolar i.e., they show low residual variance when fitted with equivalent current dipole models. They claimed that *dipolarity* serves as a proxy for physiological validity [23].

It is noteworthy that ICA results often show anatomical accuracy, despite that the algorithm is completely agnostic to the spatial structure of the input data. The emergent anatomical accuracy has been implicitly taken as evidence of the *physiological validity of ICA*. In this paper, we refer to this key assumption as *independence-dipolarity identity* (IDID). The apparent effectiveness of ICA seems to be attributed to the favorable correspondence between its underlying assumptions and the biophysical principles governing EEG generation: (1) The EEG sources are localized, stationary, temporally independent of each other, and have non-Gaussian source distributions; (2) The volume conductor theory assumes linear and instantaneous mixing process, which corresponds to matrix multiplication (which is not specific to ICA). In other words, the implicit model of ICA may closely model generative mechanism of scalp-recorded EEG coincidentally. Indeed, the pioneer group demonstrated that successful temporal (i.e., functional) decomposition of event-related potentials (ERPs) is naturally accompanied by identification of scalp projections from anatomically plausible sources [14,16,17,21,24,25], which has been echoed by other groups [26]. Today, ICA users fall into two broad camps: the majority for whom ICA stands for 'I seek artifact,' and a smaller, more committed group for whom ICA stands for 'I seek anatomy'.

Although methodological and conceptual developments emerged from the late 1990s through the mid-2000s, including high-profile journal publications such as the *Science* [14] and a summary opinion paper [19], the physiological interpretation of ICA for scalp-recorded EEG has never been subjected to critical validation. The physiological interpretation of ICA carries considerable explanatory ambition, as it purports to address the generative mechanisms of scalp-recorded EEG. Yet, in the absence of critical and systematic validation, its plausibility remains more asserted than demonstrated. To date, the status of IDID has been a qualitative and confirmatory framework, and no quantitative predictions have been made. To address this situation, we subject the model to Popperian falsification, thereby delineating the theoretical and empirical limits of ICA's physiological validity. Our strategy is outlined in the following sections.

A central yet insufficiently scrutinized aspect of the physiological interpretation of ICA is its assumed source model. Makeig and colleagues have argued that scalp-measurable EEG signals arise from a small cortical patch, a view we refer to hereafter

as the *small patch model* (Figure 1A, 1B). The historical development of this model can be summarized as follows. EEG sources were proposed to occupy compact cortical domains [14] on the order of 1 $cm^2$ [15]. This view was motivated by the observation that cortical connectivity is "very highly weighted" toward short-range (< 500 μm) connections [19], with a dominant scale near 100 μm [23]. Neurons therefore synchronize primarily with their immediate neighbors within a 100-500 μm range [27]. On this basis, ICA is thought to capture neural activity projected to the scalp from such small, locally coherent cortical patches, yielding highly dipolar scalp topographies [28]. To sum up, a spatially fully or partially coherent, $cm^2$-scale cortical patch is expected to produce a near-dipolar scalp projection patterns [29].

The small patch model has received remarkably little critical scrutiny over the past two decades. This lack of challenge, however, may not reflect broad acceptance but rather a disconnect between research communities: EEG researchers with access to alternative evidence appear simply not to have engaged with the physiological interpretation of ICA. In fact, a long-standing and repeatedly replicated estimate from the 60's places the minimum cortical area resolvable by scalp EEG at approximately 6 $cm^2$ (i.e., 1 $inch^2$) [30] . Hereafter, we will refer to this alternative view as the *large patch model* (Figure 1C). The 6 $cm^2$ minimum has been repeatedly replicated by multiple groups of epileptologists using simultaneous EEG-ECoG recordings [31–36], and simulation studies have likewise supported its validity [33,37]. Importantly, 6 $cm^2$ represents a lower bound: examining inter-ictal spikes, Tao and colleagues found that 90% of cortical spikes arising from > 10 $cm^2$ of activated cortex produced observable scalp potentials, whereas those arising from < 6 $cm^2$ never did. They concluded that synchronous activation of 10–20 $cm^2$ of gyral cortex is common [38,39], which confirmed prediction from the simulation [37].

Another counterevidence arises from cortical anatomy. In the small-patch model (Figure 1A, 1B), an active cortical patch of approximately 1 $cm^2$ is assumed to sit within a single gyral crown (yellow region). However, an average gyral span in the human cortex is only 0.45-0.55 cm through the adulthood [40]. A 1 × 1 cm patch therefore exceeds the typical width of a single gyrus and cannot be accommodated on most gyral crowns. In contrast, cortical sulci provide substantially larger surface: with an average depth of 1.3–1.4 cm and a wall-to-wall width of 0.3–0.4 cm, a single sulcus provides roughly 3 cm of continuous cortical surface from shoulder to shoulder, and the average sulcal length is nearly 700 cm [40]. Multiple 1 $cm^2$ patches could fit within this geometry. Consequently, the small-patch model predicts a strong dominance of sources arising from sulcal walls rather than gyral crowns.

Notably, proponents of the large patch model have largely been neurologists who had access to ground truth via inter-ictal simultaneous EEG-ECoG recordings and little need to rely on ICA. In addition, ICA was, especially in its early days, positioned as engineering solution requiring expertise in linear algebra and optimization theory. These

factors likely isolated the ‘I seek anatomy’ camp from the broader EEG community that might otherwise have offered critical evaluation.

In this study, we show that using ICA in the ‘I seek anatomy’ mode in fact produces results that support the large-patch model, thereby revising the physiological interpretation of ICA. As illustrated in Figure 1, the small- and large-patch models make distinct predictions regarding the depth and orientation of ICA-derived equivalent current dipoles. Our hypothesis-testing scheme relies on key anatomical facts that only one-third of the cortex lies on gyral crowns [40–42], and the average cortical thickness and sulcal depth are approximately 2.5 mm and 14 mm, respectively [40,43,44]. Given these constraints, the small-patch model predicts that one third of brain ICs should be localized to gyral crowns with small dipole angles, whereas two-thirds of ICs should be localized to sulcal walls with large angles. In contrast, the large-patch model predicts a general depth bias with predominantly small dipole angles. To determine which model is supported by data, we analyzed total of 820 datasets comprising 62- and 64-channel EEG recordings from healthy adults during eyes open and closed resting state. To demonstrate the theoretically predicted depth bias, we also conducted a simple simulation using a four-layer spherical head model, parametrically varying dipole-layer area and depth. Froward projections from the ground-truth sources were calculated, then fitted with a single equivalent current dipole to measure the depth difference between the ground truth and the estimation from the inverse solution. The volume conductor theory predicts that dipole fitting to a scalp projection arising from larger cortical patches yields systematically deeper localization bias. Table 1 summarizes the predictions by the small-patch and large-patch models.

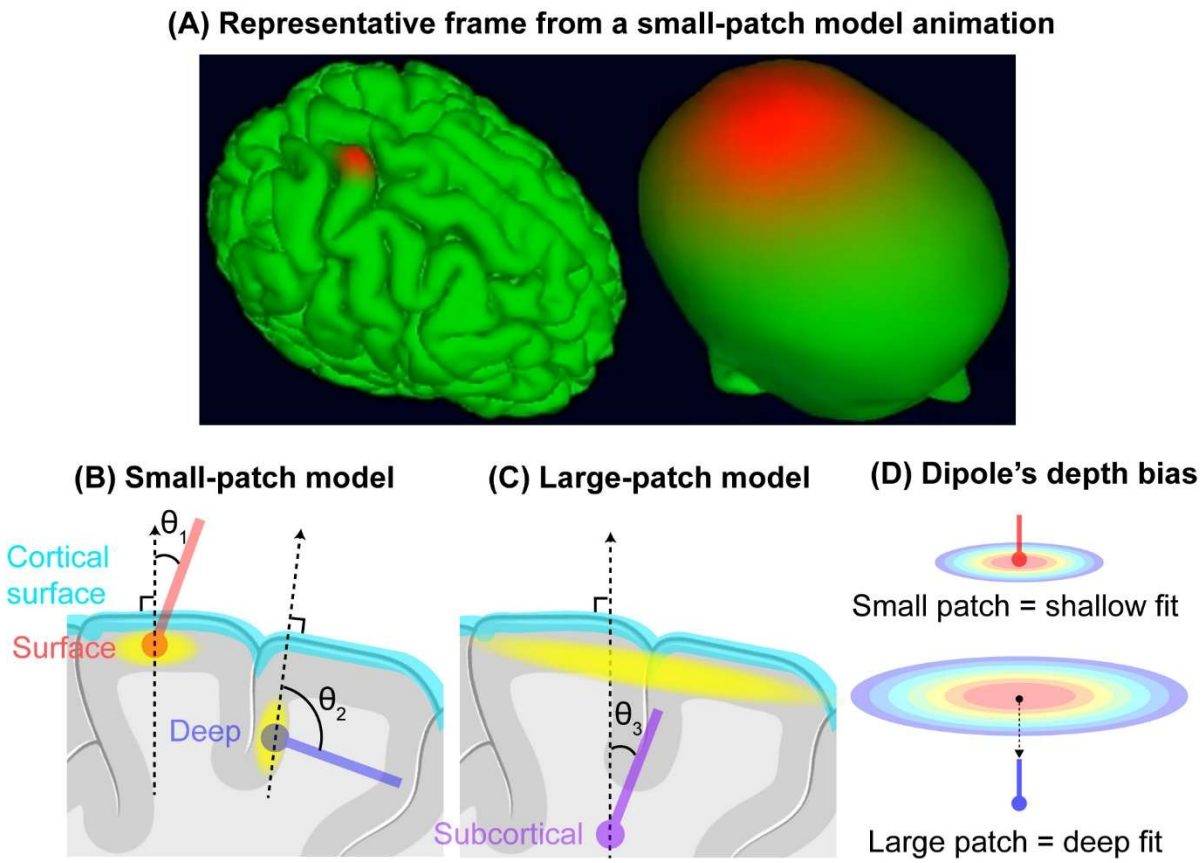


**Figure 1.** Illustration of the *small-patch* and *large-patch models* and their predicted effects on dipole depth and angles. **(A)** Screenshot from an animation of forward-model simulations generated using the Neuroelectromagnetic Forward Modeling Toolbox (NFT) [45]. The frame illustrates the scalp potential field produced by a localized cortical small-patch source. Image reproduced from a publicly available animation (Creative Commons Attribution, CC BY), available at https://youtu.be/7TP-xrVokXk (**B**) In the *small-patch model*, a synchronous cortical area smaller than a single gyral crown constitutes an EEG source. This model predicts that fitted equivalent current dipoles can distinguish gyral from sulcal sources by their depths and angles. Cortical patched highlighted in yellow represent main contributors to the scalp-recorded EEG signals. (**C**) In contrast, in the *large-patch model*, a synchronous active cortical region spans multiple gyral crowns. When such a broad source is approximated by a dipole, which is spatially idealized point with no spatial extent, the fitted dipole is displaced deeper than the actual cortical layer (the *depth bias*). This model predicts that most estimated dipoles will be radially oriented and localized significantly deeper than the layer of the neocortex. (**D**) Schematic of dipole depth bias. An equivalent current dipole is a spatially idealized point source and provides an accurate approximation for a compact cortical generator. However, when a single dipole is used to approximate a potential field produced by a broad cortical patch, which is effectively a dense array of parallel dipoles aligned with the cortical normal, the

fitted dipole is displaced to deeper locations. In this study, we refer to this systematic localization error as the *depth bias*, which we will later quantify in simulation.

**Table 1**. Comparison of predictions from the small-patch and large-patch models. Predicted observations are written in bold.

| | Small-patch model (anatomically realistic) | Large-patch model (surface dominant) |
|---|---|---|
| Source locations | **70% of sources in sulci.**<br>*Surface*: on gyral crowns<br>*Deep*: on sulcal walls<br>*Subcortical*: (non-existent) | **All in the surface (gyral crowns).**<br>*Surface*: small continua of gyral crowns<br>*Deep*: large continua of gyral crowns<br>*Subcortical*: very large continua of gyral crowns |
| Var. in IC act. | **Follows inverse-square law.**<br>*Surface*: high IC activation power<br>*Deep*: low IC activation power<br>*Subcortical*: (non-existent) | **Increases with source area.**<br>*Surface*: low IC activation power<br>*Deep*: high IC activation power<br>*Subcortical*: very high IC activation power |
| Dipole angles | **Radial at gyrus, tangential at sulci.**<br>**Spatially high-freq distribution.**<br>**Mean at 90 degrees.**<br>Surface: radial<br>Deep: tangential<br>Subcortical: (non-existent) | **Always radial.**<br>**Spatially low-freq distribution.**<br>**Mean at 0 degrees.**<br>Surface: radial<br>Deep: radial<br>Subcortical: radial |

## Materials and Methods

### Simulation Study of Serial Forward-Inverse Source Modeling

*Building a forward model.* To demonstrate the depth bias i.e. the dependence of fitted signle-dipole depth on the spatial extent of the true source, we conducted a simulation study using a 4-shell spherical head model. The radii of the cortex, cerebrospinal fluid (CSF), skull, and scalp shells were set to [7.9 8.0 8.5 9.0] cm. Lead fields were computed using the Fieldtrip function ft_compute_leadfield [46]. Sixty-four electrodes were used, with positions defined by the standard-10-5-cap385.elp montage distributed as a part of EEGLAB library. The electrodes used were Fp1, Fpz, Fp2, AF3, AF4, F7, F5, F3, F1, Fz, F2, F4, F6, F8, FT9, FT7, FC5, FC3, FC1, FCz, FC2, FC4, FC6, FT8, FT10, T7, C5, C3, C1, Cz, C2, C4, C6, T8, TP9, TP7, CP5, CP3, CP1, CPz, CP2, CP4, CP6, TP8, TP10, P7, P5, P3, P1, Pz, P2, P4, P6, P8, PO7, PO5, PO3, POz, PO4, PO6, PO8, O1, Oz, and O2. EEG sources were defined as uniform dipole layer (UDL) positioned 2 mm below the cortical surface. The radius of the UDL were parametrically varied (2, 4, 8, 16, 24, 32, 48, and 64 mm), corresponding to surface areas of 0.13, 0.50, 2.01, 8.04, 18.1, 32.2, 72.4, and 128.7 $cm^2$, respectively. To account for uncertainty in skull conductivity, we simulated three brain-to-skull conductivity ratios (BSCR = 20, 40, and 80). Conductivity values for brain, CSF, skull, and scalp were [0.33, 1.65, 0.0165, 0.33] S/m for BSCR = 20 [37,47]; skull conductivity was adjusted to 0.00825 and 0.004125 S/m for for BSCR = 40 and 80, respectively. The UDL curvature matched that of the cortical shell. Forward-model scaling was expressed in μV/(nA·m)

*Solving the inverse problem.* Dipole fitting was performed using FieldTrip [46] as implemented in the EEGLAB DIPFIT plugin. A two-stage procedure was employed, consisting of an initial coarse grid search followed by a nonlinear gradient-descent refinement. The forward-inverse solution workflow is shown in Figure 3A.

## Empirical Study of Large-Scale Resting-State EEG

### *Subjects*

We analyzed EEG data from two publicly available datasets: the Leipzig Study for Mind–Body–Emotion Interaction (Leipzig dataset; n = 212 after preselection) [48] and the Dortmund Vital Study (Dortmund dataset; n = 608) [49]. For the Leipzig dataset, the final sample included 134 males; mean age = 39.3 years (SD = 20.3). Handedness distribution was 188 right-handed, 20 left-handed, and 4 ambidextrous participants. For the Dortmund dataset, the final sample included 232 males; mean age = 44.1 years (SD = 14.5). Handedness distribution was 566 right-handed, 40 left-handed, and 2 participants with missing handedness information. Some participants completed a 5-year follow-up measurement; however, follow-up sessions were not included in the present analysis.

### *Ethics statement*

Data collection for both datasets complied with the Declaration of Helsinki. The Leipzig Study for Mind–Body–Emotion Interaction was approved by the ethics committee of the Medical Faculty of the University of Leipzig (reference number 154/13-ff). The Dortmund Vital Study was approved by the ethics committee of the Leibniz Research Centre for Working Environment and Human Factors (approval numbers A93-1 and A93-3 for the follow-up assessment). For both datasets, we confirmed upon download that all data were fully de-identified.

### *Task*

Resting-state EEG with eyes open and closed was recorded in both datasets. In the Leipzig dataset, the recording consisted of 16 alternating 1-min blocks of eyes-closed and eyes-open conditions, totaling 16 minutes. In the Dortmund dataset, the resting-state session comprised a 3-min eyes-closed block followed by a 3-min eyes-open block, totaling 6 minutes.

### *EEG recordings*

For the Leipzig dataset, scalp EEG was recorded using BrainAmp MR Plus amplifier with 62 active actiCAP electrodes (Brain Products GmbH, Munich, Germany) placed according to the international 10-10 system [50]: Fp1, Fp2, F7, F3, Fz, F4, F8, FC5, FC1, FC2, FC6, T7, C3, Cz, C4, T8, CP5, CP1, CP2, CP6, AFz, P7, P3, Pz, P4, P8, PO9, O1, Oz, O2, PO10, AF7, AF3, AF4, AF8, F5, F1, F2, F6, FT7, FC3, FC4, FT8, C5, C1,

C2, C6, TP7, CP3, CPz, CP4, TP8, P5, P1, P2, P6, PO7, PO3, POz, PO4, PO8, and FCz. FCz served as the initial reference, which was later recovered at the cost of VEOG. EEG signals were recorded online with a band-pass filter of 0.015-1000 Hz at a sampling rate of 2500 Hz.

For the Dortmund dataset, scalp EEG was recorded using BrainAmp DC amplifier with 64 active actiCAP electrodes (Brain Products GmbH, Munich, Germany) placed according to the international 10-10 system [50]: Fp1, Fp2, F7, F3, Fz, F4, F8, FC5, FC1, FC2, FC6, T7, C3, Cz, C4, T8, CP5, CP1, CP2, CP6, P7, P3, Pz, P4, P8, PO9, O1, Oz, O2, PO10, AF7, AF3, AF4, AF8, F5, F1, F2, F6, FT7, FC3, FC4, FT8, C5, C1, C2, C6, TP7, CP3, CPz, CP4, TP8, P5, P1, P2, P6, PO7, PO3, POz, PO4, PO8, TP9, TP10, FT9, and FT10. FCz served as the initial reference and was recovered by reducing the data rank by one [51]. The initial reference was FCz. EEG signals were recorded online with a low-pass filter at 250 Hz and a sampling rate of 1000 Hz.

*EEG preprocessing*

Figure 2 provides an overview of the preprocessing pipeline. EEG preprocessing was performed using Matlab R2023a (The MathWorks Inc., Natick, MA) and EEGLAB library [52] with custom code (https://github.com/MakotoMiyakoshi/DipoleDensityExtended). Raw EEG data were downsampled to 250 Hz. Canonical electrode locations on the MNI head template were assigned [53,54]. A high-pass FIR filter (Hamming window; cutoff 1.5 Hz at -6dB; 1 Hz transition bandwidth) was applied. Artifact subspace reconstruction (ASR) was performed using the EEGLAB plugin clean_rawdata, with a cutoff threshold of SD = 20 [55–61]. No other options were used in applying clean_rawdata. EEG signals were then re-referenced to the average of all scalp electrodes plus the initial reference (continuous zero channel), thereby recovering FCz as the reference electrode [51]. Adaptive mixture independent component analysis (AMICA) [62] was applied, discarding data points exceeding 3 SD during the first 15 iterations (maximum 2000 iterations) per developer's recommendation (Jason Palmer, private communication). Independent components (ICs) were classified probabilistically using ICLabel [63] into the categories of brain, eye, muscle, heart, line noise, channel noise, and other. Finally, equivalent current dipole models were fitted to each IC scalp topography (columns of the ICA mixing matrix mapped to electrode locations) using FieldTrip [46] and EEGLAB plugin fitTwoDipoles to fit symmetric bilateral dipoles where appropriate [64].

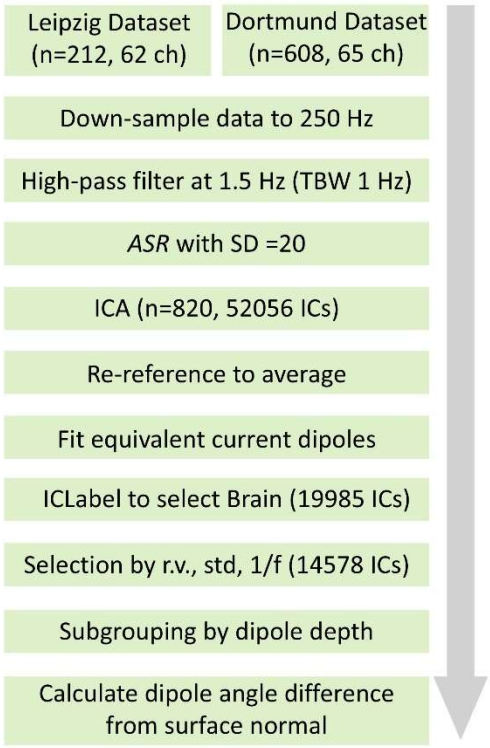


**Figure 2**. EEG preprocessing pipeline. ASR, artifact subspace reconstruction; ICA, independent component analysis; r.v., residual variance; std, standard deviation.

*Head model preparation*

For EEG source-model analysis, we used the ICBM152 template head model included with EEGLAB (avg152t1.mat). This anatomical template represents the averaged T1-weighted MRI of 152 healthy young adults (ages 18.5–43.5 years) acquired at the Montreal Neurological Institute as part of the International Consortium for Brain Mapping (ICBM) project [65,66]

Anatomical labeling was performed using the Automated Anatomical Labeling (AAL) atlas [67] as implemented in the ROI_MNI_V4.nii file distributed with FieldTrip [46]. Because our analysis did not require internal compartment boundaries (e.g., ventricular walls or cerebellar interfaces), we manually edited lower axial slices (z = -26 to -12 mm) to close deep sulcal clefts and ventricular/cerebellar cavities, yielding a topologically spherical and approximately convex cortical volume. This customized cortical model was then expanded to match the spatial extent of the EEGLAB's template head model ICBM152 on a slice-by-slice basis (see Figure S1 in Supplement). The resulting atlas was thus coregistered to the EEGLAB's head model used for dipole fitting. Dipole depth and orientation (angle relative to the cortical surface normal) were computed with respect to the surface mesh derived from this customized cortical model. Subcortical regions were defined according to the AAL atlas and included 43 labels encompassing

the following structures: olfactory cortex, insula, hippocampus, parahippocampal gyrus, amygdala, caudate, putamen, pallidum, thalamus, and all cerebellar regions.

*EEG analysis*

Power spectral density (PSD) for IC activations was computed from 2 to 45 Hz in 0.1-Hz steps using MATLAB's stft function with a 1-s Hamming window and 50% overlap. For robustness against outliers, the median across time windows was used instead of the mean. The spectral exponent coefficient $\alpha$ of the $1/f^{\alpha}$ spectrum was estimated using FOOOF [68] with the following parameters: aperiodic_mode = 'fixed', max_peaks = 1, min_peak_height = 0, peak_width_limits = [0.5 4], proximity_threshold = 0, peak_type = 'best', guess_weight = 'weak', hOT = 1, and thresh_after = true. The resulting exponent $\alpha$ from the $1/f^{\alpha}$ fit was later used for quality control. The standard deviation of each IC activation time series was computed to examine the relationship between dipole depth and signal amplitude. Finally, residual variance from dipole fitting was also obtained for both quality control and evaluation.

ICs labeled as "brain" by ICLabel were further screened according to the following criteria:

(1) residual variance of dipole fitting < 0.15
(2) IC activation power falls between the 0.1 and 99.9 percentiles
(3) spectral exponent coefficient α > 0.4. (Figure 4D)

ICs meeting all criteria were retained as the final Brain class and subdivided into three depth-based categories:

(1) Surface cortex: –5 to +10 mm relative to the cortical surface
(2) Deep cortex: AAL-defined cortex (beyond +10 mm)
(3) Subcortex: AAL-defined subcortical structures

*Interpretation of the AAL-defined cortex.* It is important to note that the AAL-defined cortex is substantially thicker than actual human gray matter. Empirically, mean cortical thickness in the human brain is approximately 2.5 mm [40]. In contrast, an axial slice of our modified cortical AAL mask at z = -20 mm (Figure 4E) shows a mean thickness of 23.6 mm (SD = 6.2; range: 8.9-44.0 mm). As a result, the AAL-defined cortex encompasses substantially large portions of white matter and subcortical tissue. The broad spatial extent would be useful for absorbing individual differences in gyrification and for mitigating modeling errors. However, for the purpose of estimating equivalent current dipole depth, it permits dipoles to be labeled as "cortical" even when they fall far deeper than is physiologically plausible. For this reason, we treat the AAL-defined cortex as "Deep cortex": dipole

sources falling within this region should already be regarded as implausibly deep, despite the anatomical label “cortex.”

*Software development and dissemination*

For this study, we developed EEG_Clustering, an EEGLAB plugin extension for group-level analysis and visualization of spatiotemporal properties of ICs. The tool serves as an alternative to the EEGLAB STUDY framework by enabling IC clustering based on estimated dipole coordinates. It provides visualization of IC dipole-density distributions within the MNI template head space, as well as group-level summaries of associated time–frequency and spectral characteristics. The tool is available from https://github.com/kkukka21/EEG_Clustering and dedicated documentations are available in Supplement.

## Results

### Simulation Study of Serial Forward-Inverse Source Modeling

The forward-inverse simulation demonstrated depth bias in single-dipole fitting (Figure 3). As expected, this simple simulation revealed the area-depth dependency when using a single-dipole model. The overall residual variance was < 2% (for detail, see Supplement). We concluded that the large-patch model explains the depth bias when a single current dipole model is fitted.

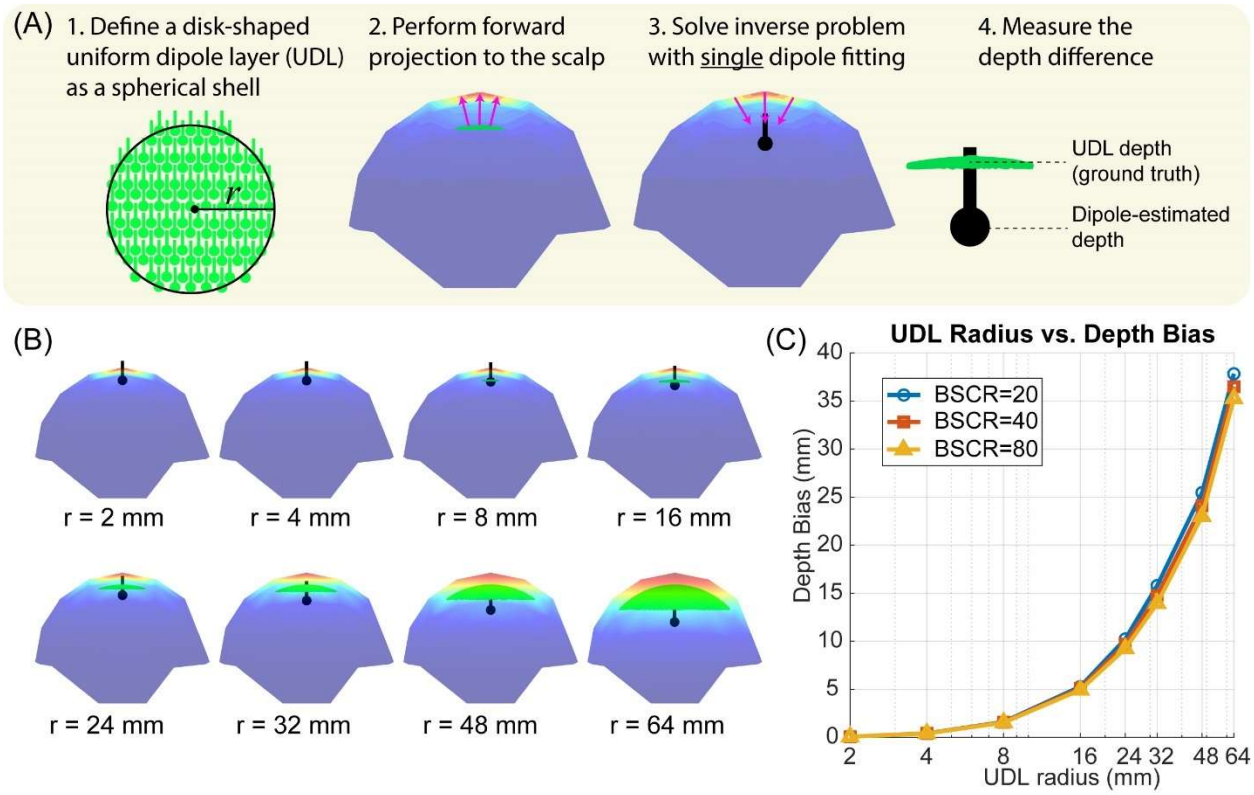


**Figure 3**. Forward-inverse simulation demonstrating depth bias in single-dipole fitting. A four-shell spherical head model was used with radii for the brain, cerebrospinal fluid (CSF), skull, and scalp set to [7.9 8.0 8.5 9.0] cm, respectively. Tissue conductivities were [0.33, 1.65, 0.0165, 0.33] S/m for the brain-to-skull conductivity ratio (BSCR) of 20; skull conductivity was adjusted to 0.00825 and 0.004125 S/m for BSCR values of 40 and 80, respectively. (**A**) Schematic of the simulation design. First, a disk-shaped uniform dipole layer (UDL), conforming to the curvature of the brain shell was defined with parametrically varied radii. The UDL depth was fixed at 2 mm below the brain surface and served as ground-truth source depth. Dipole orientations were set normal to the brain surface, with an inter-dipole spacing of 1.5 mm and unit dipole moments μV/(nA·m). Second, scalp potentials were generated via forward projection by computing lead fields from the UDL to 64 simulated scalp electrodes. Third, the resulting scalp topography was fitted using a single equivalent current dipole model. We predicted that broader source regions would yield systematically deeper estimated dipole locations. Finally, depth bias was quantified as the difference between the estimated dipole depth and the true UDL depth. In the schematic, the upper hemisphere rendered with a red-yellow-blue color scale represents the scalp potential distribution, the green convex disk represents the UDL, and the black disk-and-stem denotes the fitted dipole. For visual clarity, the UDL depth in (A) is exaggerated. (**B**) Estimated dipole locations for increasing UDL radii (r = 2–64 mm), demonstrating progressively deeper fitted dipoles despite constant source depth. (**C**) Radius-dependent depth bias across three BSCR conditions. Depth bias increases monotonically with UDL radius and is robust across skull conductivity assumptions.

## Empirical Study of Large-Scale Resting-State EEG

*Extracting preselected brain components*

Across the 820 datasets, we obtained 52,056 ICs, of which ICLabel identified 19,985 as Brain class candidates (Figure 4A). After applying our additional quality-control criteria (Figure 4D shows one of them), 14,578 ICs remained for the final analysis (Figure 4B). Class-wise IC activation power analysis showed that excluded Brain-class ICs exhibited substantially lower power than retained ICs, indicating that they were non-dominant in amplitude (Figure 4F).

*Depth-based classification and characterization*

The retained Brain ICs were divided into three depth-based subgroups: Surface cortex (19.7%), Deep cortex (52.6%), and Subcortex (27.6%) (Figure 4C, G–H). Notably, more than 80% of the qualified Brain ICs were localized deeper than 5 mm, a depth range that is physiologically implausible for scalp-measurable cortical generators. Depth-wise IC activation power and residual-variance analyses further showed that Surface-cortex ICs tended to have lower power and higher residual dipole variance, indicating that ICs with surface dipoles were generally of poorer quality.

The results of the depth analysis are consistent with the large-patch model: the small-patch model cannot account for the predominance of deep dipole locations produced by ICA. Strikingly, 27.6% of the qualified Brain ICs were localized within Subcortical regions, a depth exceeding even the already extended AAL-defined cortical mask, whose average thickness is approximately 23 mm at $z = -20$. This substantial proportion of subcortical dipoles underscores the incompatibility of the small-patch model with empirical ICA outcomes. Moreover, the combination of lower IC activation power and higher residual variance observed in Surface-cortex ICs indicates that these components represent a nondominant portion of the ICA decomposition and are generally of poorer quality. In contrast, the result suggests that high-activation power, low–residual-variance ICs are localized deeper in the brain, mostly subcortical.

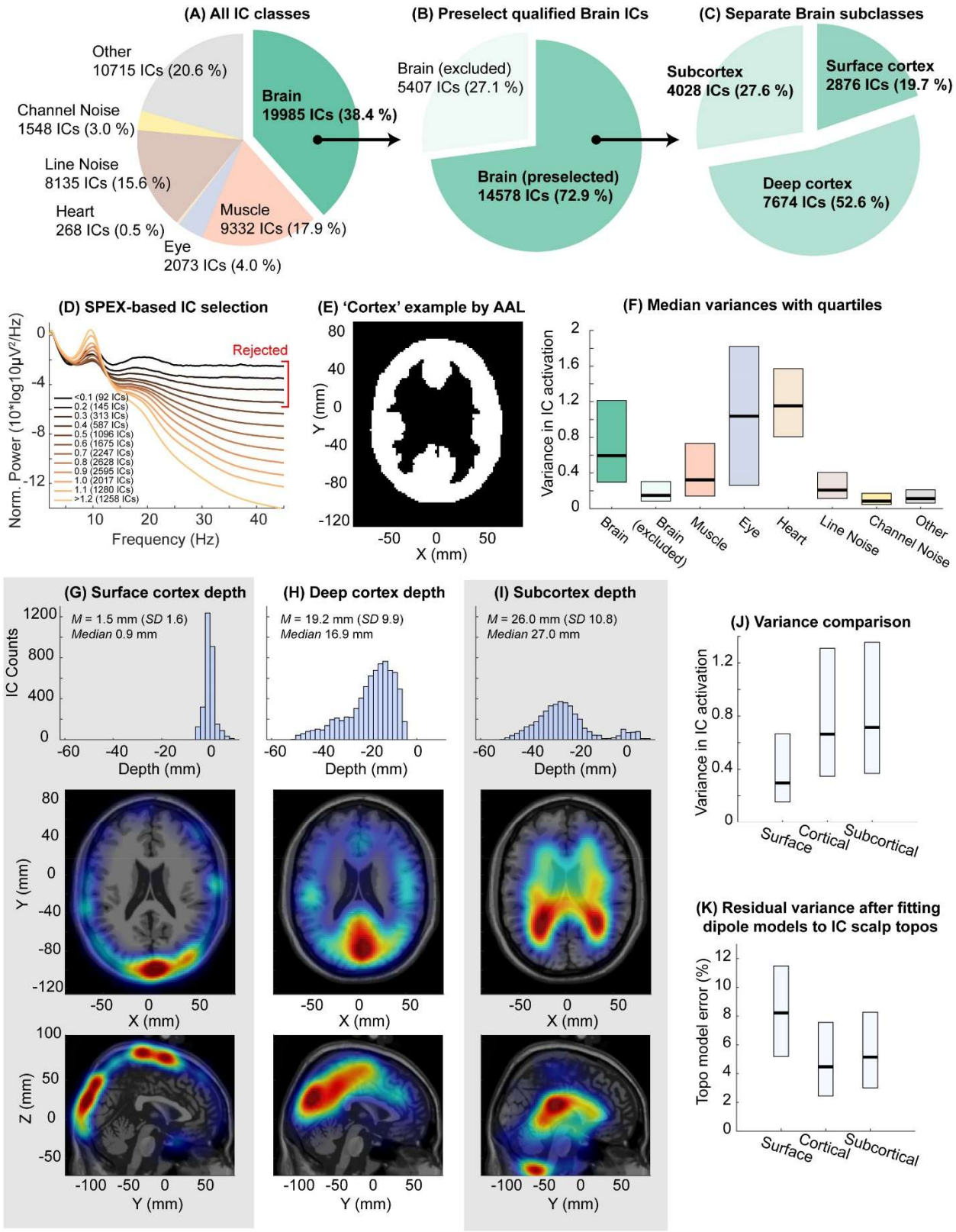


**Figure 4**. Selection of qualified Brain-class independent components (ICs) and summary statistics for spatiotemporal measures from 52,056 ICs across 820 EEG datasets. (**A**) Distribution of ICLabel classes. For each IC, the class with highest posterior probability was

adopted. (**B**) Preselection of the Brain-class ICs using the following quality criteria: residual variance of dipole fitting < 0.15; robust-estimated IC activation power within the 0.1-99.9 percentile range; spectral exponent (SPEX) coefficient > 0.4; and dipole depth within +10 mm of the cortical surface. The resulting 14,578 ICs are hereafter referred to as the Brain class. (**C**) The Brain class was subdivided into three depth-based subclasses: *Surface cortex* (depth -5 to +10 mm relative to the cortical surface), *Deep cortex* (deeper than -5 mm and labeled as cortical by AAL), and *Subcortex* (outside AAL cortical labels). (**D**) Mean power spectral density (PSD) across SPEX bins, each spanning a 0.1 interval. ICs with SPEX < 0.4 showing relatively flattened spectra were rejected, whereas higher SPEX values exhibit neurophysiologically valid low-pass spectra consistent with predictions by cable theory. (**E**) Example of an AAL cortical mask (axial slice at *z* = 20 mm). The cortical mask's thickness in this slice (M = 23.6 mm, SD = 6.2; range: 8.9-44.0) far exceeds the true gray-matter thickness (2-4 mm), illustrating an overly lax spatial definition of "cortex" used in the current study. (**F**) Median IC activation power with interquartile ranges for each class. The Brain class is shown separately for qualified and excluded ICs for comparison. (**G-I**) Dipole depth distributions (top row) and location density maps (middle row: axial slice at *z* = 20mm; bottom row: sagittal slice at *x* = 0 mm) fur Surface, Deep, and Subcortical subclasses. Color limits (left to right panels): [0 0.05], [0 0.2], [0 0.1]. (**J**) Median and interquartile ranges of IC-activation power for the three subclasses. (**K**) Median and interquartile ranges of residual variance after fitting dipole to IC scalp topographies. Smaller values indicate less errors.

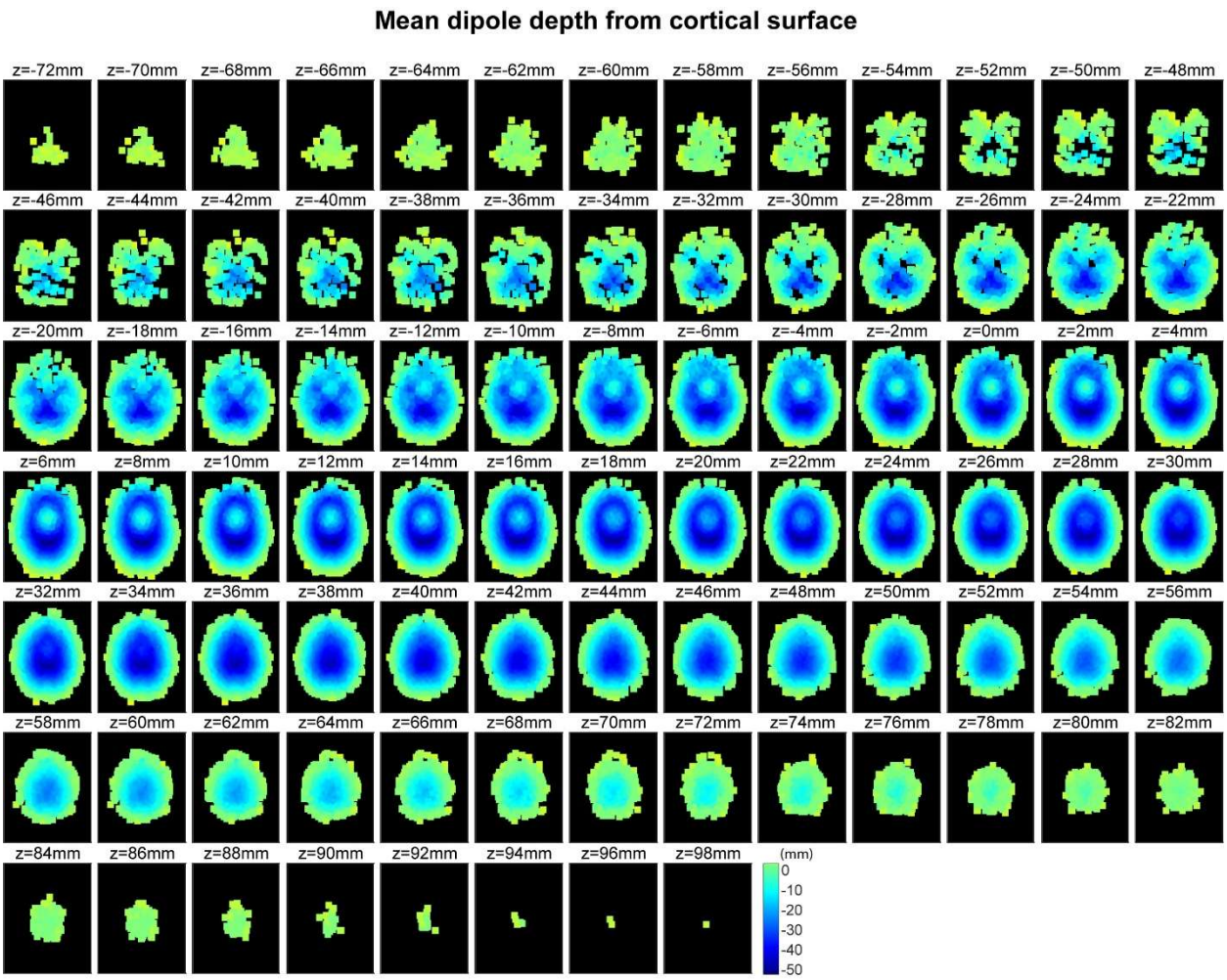


**Figure 5**. Mean dipole depth relative to the cortical surface, visualized across axial slices. Depth estimates were smoothed using a Gaussian kernel with σ = [2 2 2] mm.

*Depth tomography*

Distribution of dipole depth within the brain space is visualized in Figure 5. It is noticeable that for axial slices in z >= 30 mm, the depth distribution is mostly concentric, while in 16 < z < 30 mm, a small island of low-depth region appears in the frontal region. The frontal island of the low-depth region was due to void occupying the position of basal ganglia, thalamus, and ventricle that was not filled in by manually tailoring the bottom slides.

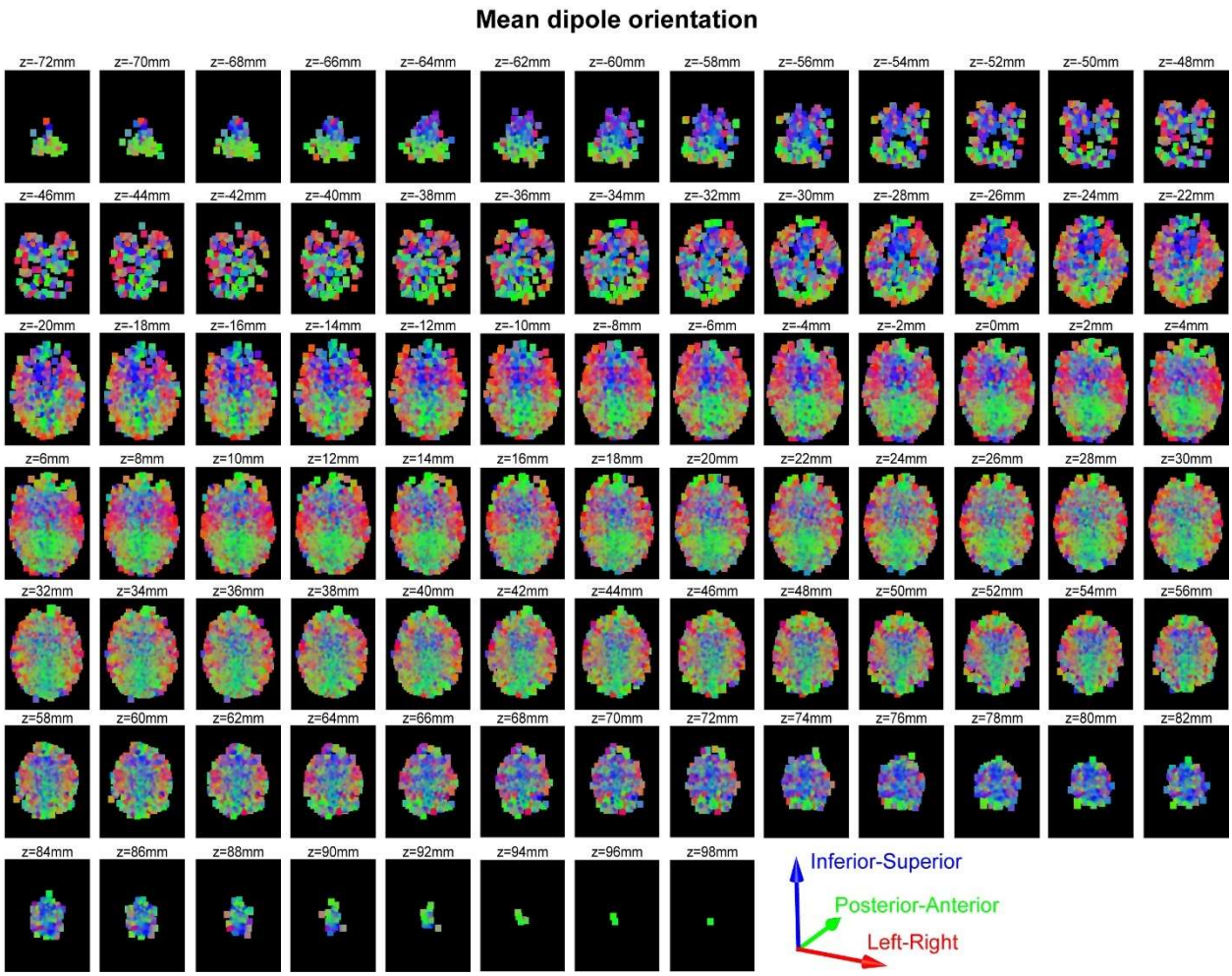


**Figure 6**. Mean dipole orientations, visualized across axial slices. The angles were smoothed using a Gaussian kernel with σ = [2 2 2] mm.

*Orientation tomography*

The spatial distribution of dipole orientations across the brain is visualized in Figure 6. The small-patch model predicts that the orientation pattern should reflect the high spatial frequency of cortical gyrification. Given that the average gyral width is only 0.45–0.55 cm, which is approximately 3–4% of the 15–20 cm anterior–posterior brain axis, local cortical normals should rotate rapidly across the surface. Consequently, the small-patch model leads to a prediction of a highly heterogeneous, fine-grained, and nearly randomized pattern of dipole orientations throughout the brain volume. The empirical ICA-derived orientation tomography shown here however exhibits a clear contrast: broad, coherent, and low–spatial-frequency structure, which supports the large-patch model than the small-patch model.

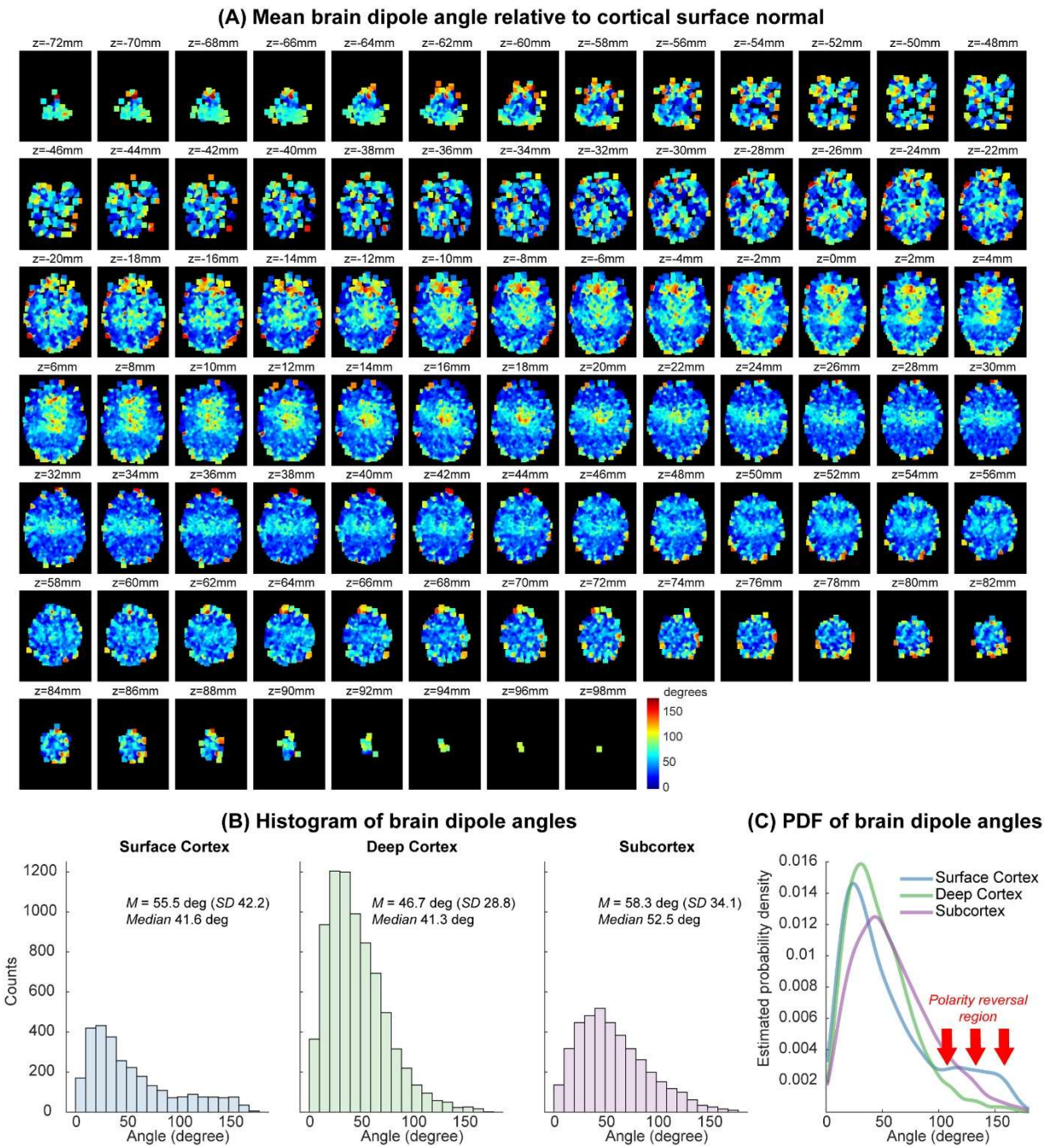


**Figure 7**. Summary of dipole angle differences relative to outward cortical surface normal for 14,578 Brain-class ICs. **(A)** Mean dipole angle differences visualized across axial slices. The angles were smoothed using a Gaussian kernel with σ = [2 2 2] mm. Angles are expressed relative to the local outward cortical normal (0° = outward radial; 90° = tangential; 180° = inward radial). Lower angles (blue) are more frequently observed within the brain volume, whereas higher angles (yellow-red) are found near the cortical boundary. **(B)** Histograms of dipole angles for three depth-based subclasses: Surface cortex, Deep cortex, and Subcortex. **(C)** Estimated probability density functions (PDFs) of dipole angles for the three subclasses derived from normalized histograms with 100 bins. The Surface cortex distribution shows a secondary peak

above 100°, replicating polarity reversal associated with poor signal quality (Miyakoshi et al., 2023).

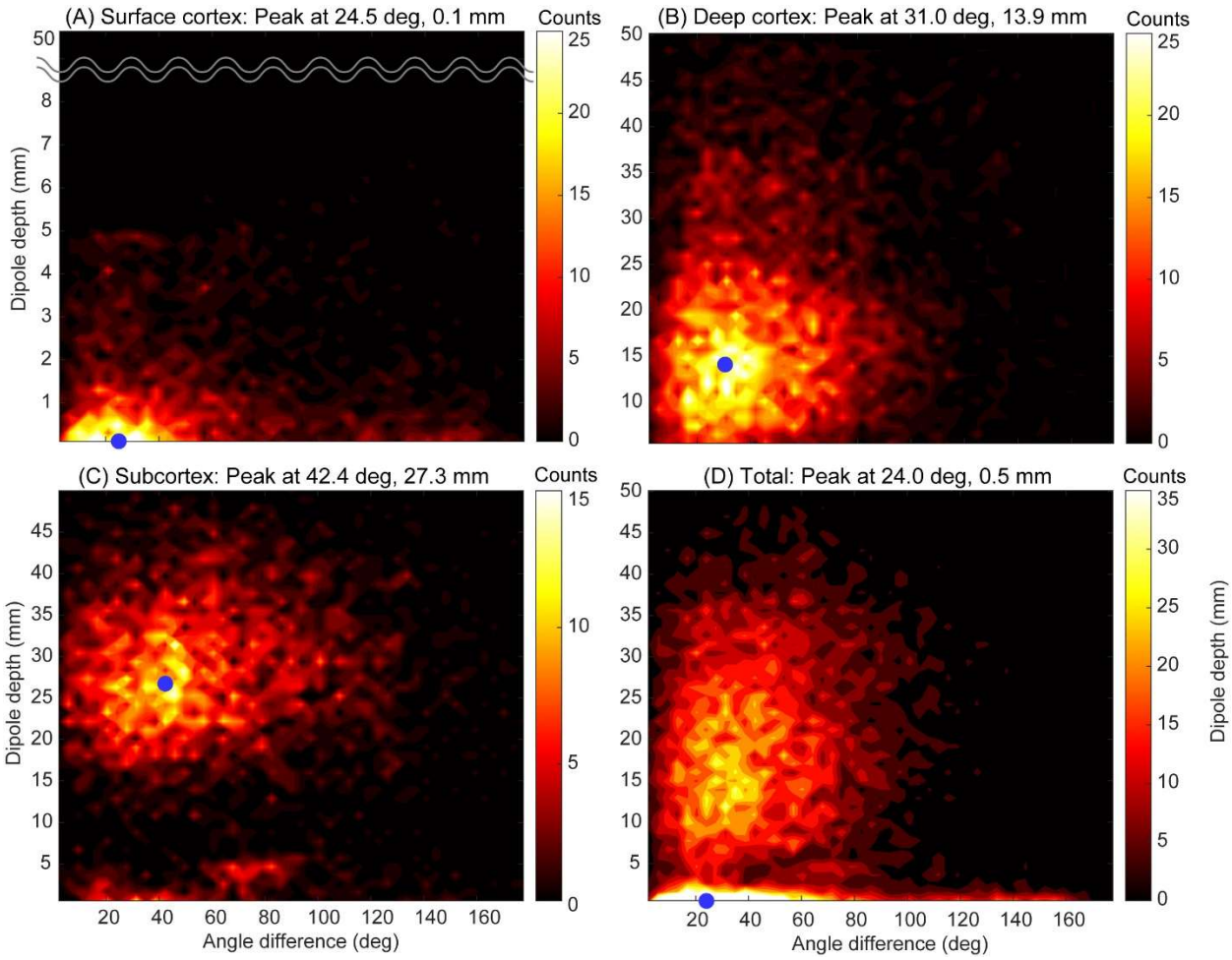


**Figure 8**. Joint histogram of dipole depth and angle relative to the outward cortical surface normal. Joint histograms are shown separately for (**A**) Surface cortex, (**B**) Deep cortex, (**C**) Subcortex, and (**D**) all subclasses combined. The blue dot marks the location of peak density in each panel. Note that the depth axis in (**A**) is magnified fivefold relative to other panels.

*Angle-difference tomography and angle–depth relations*

The small-patch model predicts a step-function–like increase in dipole angle, shifting abruptly from radial orientations at gyral crowns to tangential orientations along sulcal walls (≈15 mm deep). In contrast, the empirical angle tomography in Figure 7A reveals a broad angle plateau across much of the intracranial volume, with only minor, gradual angle change across depth tiers. This spatially low-frequency pattern is more consistent with a large-patch model than with the sharply depth-dependent behavior predicted by the small-patch model.

A prominent horizontal band of increased angles spanning approximately z = 16–56 mm may correspond to the anatomical course of the central sulcus (Rolandic fissure), which is a region whose time–frequency signatures is often characterized as the μ rhythm to which ICA is

notably sensitive. This observation further supports the view that anatomical curvature, rather than depth per se, is the principal driver of dipole-angle variability.

Another key departure from small-patch model predictions was that sulcal generators were expected to exhibit dipole angles clustered near 90°, yet the empirical histograms in Figure 7B–C showed median angles only in the 41–53° range across all depth tiers. This consistent dominance of moderately oblique orientations suggests the influence of additional, unresolved sources of angle variation at mesoscopic–macroscopic scales which were not captured by either the small-patch or large-patch idealizations. An alternative possibility was that the framework of dipole angle calculation had a systematical bias which we are unaware of.

To examine the relationship between dipole angle and depth, we generated joint angle–depth histograms (Figure 8). These distributions justifieded the reason why Surface cortex needs to be as a distinct tier: its angle–depth structure is sharply localized near the cortical sheet. In contrast, the joint distributions for Deep cortex and Subcortex form a continuous, overlapping manifold, indicating that the boundaries imposed by the AAL-based subgrouping are arbitrary and not justified by the current data structure. This continuity further supports the large-patch model, in which the dipole depth is determined by the spatial extent of the contributing source region rather than an actual generative mechanism of EEG signals constrained in a thin gray matter on the surface of the brain.

Taken together, the empirical angle structure exhibits neither the depth-linked transitions nor the sulcal tangential dominance predicted by the small-patch model, further underscoring the need for models that incorporate whole-brain anatomical curvature and mesoscale field geometry.

*Validating the predictions of the small-patch model*

Across all analyses reviewed above, Tables 2–5 summarize the extent to which the predictions of the small-patch model were supported or contradicted by the large-scale empirical database. In nearly every case, the small-patch model failed to account for the observed distributions of dipole depth, orientation, or angle–depth structure. One of the few apparent successes was the presence of a very narrow peak of shallow dipoles (+10 to –5 mm relative to the cortical surface) in the depth histogram (Figure 4G). However, this result comes with an important caveat: the Surface cortex tier consistently exhibited lower activation power and higher residual variance, indicating poorer signal quality and weaker dominance in the ICA mixing process. Consequently, the dipoles that are superficially consistent with small-patch predictions arise from components that are less physiologically credible, which is practically a part of the decomposition to ‘make ends meet’ after obtaining dominant components.

Thus, if we look for brain signals among ICs that have dominant amplitude and clear spatiotemporal characteristics i.e., physiological validity, we would inevitably find them from those localized to physiologically implausible depth. This constitutes a central irony that has gone undiscussed in the two decades of adopting ICA for physiological interpretation.

**Table 2**. Small-patch model predicted versus observed dipole-depth rates. A substantial proportion of dipoles were localized within AAL-defined subcortical regions, a finding that the small-patch model cannot account for.

| | Dipole depth rate | | |
|---|---|---|---|
| | Predicted by Small-patch model | Observed | Mean depth |
| Shallow | 30 % | 19.7% (2876 ICs) | 1.5 mm (SD 1.6) |
| Deep | 70 % | 52.6 % (7674 ICs) | 19.2 mm (SD 9.9) |
| Subcortical | 0 % | 27.6 % (4028 ICs) | 26.0 mm (SD 10.8) |

**Table 3**. Small-patch model predicted versus observed IC activation power.

| | IC activation power | |
|---|---|---|
| | Predicted by Small-patch model (inverse-square law) | Observed |
| Shallow | Large | *M* = 0.61 (*SD* 0.94), *Median* 0.30 |
| Deep | Small | *M* = 1.12 (*SD* 1.50), *Median* 0.66 |
| Subcortical | Non-existent | *M* = 1.20 (*SD* 1.67), *Median* 0.71 |

**Table 4**. Small-patch model predicted versus observed residual variance after fitting dipole models to IC scalp topographies.

| | Residual variance | |
|---|---|---|
| | Predicted by Small-patch model | Observed |
| Shallow | Small | *M* = 8.26 % (*SD* 3.79), *Median* 8.22 |
| Deep | Large | *M* = 5.35 (*SD* 3.51), *Median* 4.48 |
| Subcortical | Non-existent | *M* = 5.90 (*SD* 3.52), *Median* 5.15 |

**Table 5**. Small-patch model predicted versus observed dipole angles relative to outward cortical-surface normals. The peak values refer to joint histograms in Figure 8.

| | Dipole angles relative to cortical surface normal | |
|---|---|---|
| | Predicted by small patch model | Observed |
| Shallow | Small | *M* = 55.5 deg (*SD* 42.2), peak 24.5 |
| Deep | Large | *M* = 46.7 deg (*SD* 28.8), peak 31.0 |
| Subcortical | Non-existent | *M* = 58.3 deg (*SD* 34.1), peak 42.4 |

## Discussion

In this study, we attempted to determine the physiological interpretation of ICA applied to scalp-recorded EEG. To this goal, we compared the small-patch source model proposed by early ICA proponents with the large-patch model supported by neurologists and theorists. Using two European resting-state EEG databases, we analyzed the distributions of ICA-derived dipole depth and their relationships to IC activation power, residual variance, and dipole orientation. Across these measurements, empirical results consistently favored the large-patch model over the small-patch model. Below, we discuss the implications of these findings point by point.

*The significance of the current study*

The original physiological interpretation of ICA proposed by Makeig and colleagues rests on the small-patch source model [14,15,19,23,27–29], an assumption that has remained largely unvalidated for more than two decades, despite presence of counterevidence [31–39]. To our knowledge, the present study is the first to explicitly interrogate this core premise and to subject it to systematic falsification. Notably, despite the widespread adoption of ICA for artifact rejection, its use for extracting putative brain sources has remained limited. One plausible reason is that the physiological interpretation of ICA critically relies on dipolarity and the associated IDID, yet ICA-derived dipole fits frequently yield physiologically implausible depths, which is a pattern we confirmed in over 80% of qualified brain components in this study. Such results must have puzzled researchers attempting anatomical interpretation, in addition to the more technical challenge of post-ICA inter-subject inconsistency. This perspective also helps explain why ICA has historically been less integrated with distributed source modeling frameworks: dipolarity is inherently a property of single-dipole fitting and does not extend to distributed source models.

In the context of distributed source modeling, it typically impose a gray-matter constraint on source locations. In contrast, our dipole fitting does not impose any constraint on the location of fitted dipoles. Although the gray-matter constraint is physiologically motivated and computationally useful for solving the inverse problem, it carries the risk of prematurely discarding informative structure present in minimally constrained model outputs. The present study demonstrates the value of a minimally constrained model by examining outputs that may initially appear physiologically implausible. As shown in Figure 6 and 7, dipoles localized at implausible depths nevertheless exhibited systematic, spatially organized low-frequency patterns. This observation argues strongly against the superficial dismissal of deep dipoles. In fact, these deep dipole sources showed higher signal power and lower residual variance, indicating greater dominance and better model fit than superficially localized, physiologically plausible dipole sources. These observations caution against a bias toward hasty physiological interpretation. Rather, judgment should be suspended (i.e.,

Husserlian *epoché*) until the full set of observations can be accounted for in light of basic anatomy and electrophysiology established in the literature. Finally, the presence of a systematic bias should not be regarded as bad as it may appear because it points to regularity in the underlying generative mechanism producing the error, like the case of the dipole's depth bias we clarified using simulation.

Finally, beyond being the first attempt to explicitly falsify the small-patch model, the present study did so by adhering closely to the original methodological framework proposed by Makeig and colleagues themselves. We employed the same analysis tools and criteria used in prior ICA-based work, but examined aspects that have received little attention, namely dipole depth and orientation. By applying the original approach to previously unexamined dimensions of the data, we falsify the small-patch hypothesis while remaining fully within its methodological boundaries, following a direct proof-by-contradiction approach that contributes to clarity of our argument.

*Small-patch manifesto*

We selected a paragraph from Akalin Acar and colleagues [29] that we believe most clearly articulates the physiological concept underlying the small-patch model. It is a lengthy passage, but because it is central to the argument, we reproduce it in full below without modification.

> More formally, we assume that each IC source represents a far-field projection to the electrodes of local cortical field potentials that are fully or partially coherent across a single small cortical domain or patch of unknown size and shape. In large part because of the extreme preponderance of short-range corticocortical connections (≤100 μm), wholly so for inhibitory neurons and glia, and the predominance of tight radial thalamocortical loops, both supporting oscillatory local field dynamics, models of cortical field dynamics (Deco et al., 2008) demonstrate the emergence of such patches or islands of cortical local field synchrony likened to "pond ripples" by Freeman (2003) and to recurring (point spread) avalanches by Beggs and Plenz (2004). Thus, brain connectivity both favors the emergence of temporal synchrony within small, connected cortical domains and minimizes temporal synchrony between such domains other than in exceptional locations and circumstances. Because of the common alignment of cortical pyramidal cells perpendicular to the cortical surface, spatially coherent local field activity across such a patch will have a non-negligible far field projection to the scalp (Baillet et al., 2001; Nunez and Srinivasan, 2006), forming an effective EEG source whose time course may typically be near statistically independent of the time courses of concurrent far field potentials generated by other, spatially separated cortical source patches.

Within this passage, the second sentence is of particular importance. At the same time, it is syntactically dense and conceptually layered. Focusing on this key sentence, we can simplify the argument as follows:

> Because of the preponderance of short-range corticocortical connections (≤100 μm) and the predominance of radial thalamocortical loops, models of cortical field dynamics (Deco et al., 2008) demonstrate the emergence of small and compact cortical patches.

In the following sections, we refer to this quote as *small patch manifesto,* and examine its validity.

*Where did the small patch model come from, and what does it miss?*

The small-patch model was motivated by electrophysiological studies conducted at microscopic spatial scales (≈100-1000 μm), including recordings from inhibitory [69] and excitatory neurons [70,71] in the visual cortex of cats and macaques. These studies characterized the distribution of cortico–cortical lateral connection distances and emphasized the predominance of short-range connectivity such as ≤100 μm [23] and < ≤500 μm [19]. From this microcircuit perspective, Makeig and colleagues inferred that EEG-measurable sources should arise from spatially compact cortical patches.

While this inference is intuitively appealing, it overlooks a critical property of population-level field generation that relatively small fractions of synchronized neurons can dominate macroscopic electrophysiological signals. Empirical and theoretical studies have shown that as little as 1% of pyramidal neurons within a cortical area of 1 cm² can account for approximately 96.5% of the observed signal power [72,73]. This counterintuitive effect arises from the nonlinear scaling of synchronous versus asynchronous contributions in large neuronal populations. To illustrate this point quantitatively, consider that the human cerebral cortex contains 22.9 billion neurons distributed across approximately 1,883 cm² of surface area in average man [43,44], with roughly 85% being pyramidal neurons [74]. This yields an estimate of approximately 10 million neurons per cm², which is remarkably similar to corresponding estimates in macaque visual cortex [75]. A synchronized subset comprising just 1% of this population corresponds to 100,000 neurons, whereas the expected amplitude of random, uncorrelated activity scales with the square root of the population size corresponds to 3162 neurons. Thus, 1% of synchronous neurons can produce 31.6 times larger signal than the background noise. The underlying simple mathematics shows that the contribution of a synchronized fraction always exceeds that of the entire population acting asynchronously once the number of neurons go beyond a critical mass ($0.01x > \sqrt{x}$, $x > 10000$), which is only modest in the spatial scale of EEG [76].

Independent empirical support for this sparse-synchrony, large-area view comes from the classic work of Walter [77]. Using human intracranial EEG recordings, Walter observed that sensory-evoked responses rarely exceeded 30 μV, whereas direct electrical stimulation of the same cortical regions could elicit highly localized after-discharges of 1–3 mV, confined to only a few cubic millimeters of cortex. Interpreting

these after-discharges as an analogue of “fully coherent” activation (as in the small-patch manifesto) of the local neuronal population, Walter inferred that sensory-evoked responses engage on the order of 1% of neurons at any given cortical locus. The comparison on brain potentials between spontaneous field oscillation and that caused by electrical stimulation was replicated immediately [30]. Walter concluded that:

> The conclusion is that a signal from any receptor, even if due to maximal sensory stimulation, can activate only about one neuron in a hundred in frontal cortex, but will have this effect over a vast surface containing several thousand million neurons. All significant sensory stimuli therefore […] must be considered as activating some tens of millions of neurons over a very extensive area, without necessarily intruding on any other afferent signals or background activity.

The scaling relationship reviewed above implies that scalp-recorded EEG is extremely sensitive to fluctuations in neural synchrony, and that this sensitivity grows rapidly with the spatial extent of the contributing cortical population. In contrast, the absolute synchrony rate becomes progressively less important as population size grows. By focusing on micro-scale connectivity and absolute synchrony rates, the small-patch model overlooked this fundamental population-level property of field summation, thereby underestimating significance of the effective spatial extent of EEG-generating sources. Instead, scalp-recorded EEG is more plausibly dominated by weak neural synchrony distributed across large cortical patches (> 10 $cm^2$ [38,39], corresponding to neural populations of > 100 million neurons [43,44,74,75]), with synchrony rate less than a few percent [72,73]. This scaling law is both unique and critical to scalp EEG research, and fundamentally distinguishes it from invasive electrophysiological modalities.

Finally, we must note that key support for the small-patch model rests in part on misrepresentation of prior anatomical and modeling studies. For example, in the small patch manifesto, work by Deco and colleagues is cited as evidence that an extreme preponderance of short-range corticocortical connections (≤100 μm) supports a compact source model. However, Deco and colleagues explicitly stated that “Intracortical fibers are mostly unmyelinated and extend laterally up to 1 cm (in the human brain) with excitatory and inhibitory connections.” [78] Their work contains no analysis or claim linking the prevalence of ≤100-μm connections to the emergence of small patches of EEG sources. A second representative example appears in Delorme and colleagues [23], who argued:

> There are strong biological reasons to believe that under favorable circumstances ICA should separate signals arising from local field activities in physically distinct, compact cortical source areas: First, short-range (<100 μm) lateral connections between cortical neurons are vastly more dense than longer-range connections [3, 4]…

Reference [4] in this passage is the work of Stepanyants and colleagues [71]. However, Stepanyants and colleagues summarized their findings quite oppositely: “excitatory connectivity in cat area 17 is highly nonlocal; 74% of excitatory synapses near the axis of a 1,000-μm-diameter cortical column originate from neurons located outside the column.” Thus, explicitly nonlocal connectivity (>1,000 μm) was cited as evidence for local connectivity (<100 μm). These examples constitute clear cases of misleading citations. Nevertheless, such errors have persisted for more than a decade and continue to reinforce the small-patch model. This persistence is unlikely to reflect widespread acceptance of the anatomical claims. Rather, it represents a structural indifference and disconnect between research communities: microcircuit electrophysiologists do not read ICA-focused technical papers dedicated for scalp EEG, while EEG researchers do not read microcircuit papers because they do not scale to scalp EEG directly. As a consequence, cross-field verification has been absent. We haven’t executed exhaustive search on all such cases, but we urge caution for future readers when reading anatomical claims propagated through citations in the small-patch model literature.

*The significance and impact of refutation of the small-patch model.*
How much does refuting the small-patch model undermine the physiological interpretation of ICA? We argue that the impact is limited because IDID [23] is independent of the assumption of the source model and remains intact. That said, the refutation directly impacts the work of Simultaneous Tissue Conductivity and Source Location Estimation (SCALE) [29]. In this framework, skull conductivity is parametrically varied to identify a solution that minimizes the estimated cortical source patch size. While the methodological idea is innovative, the justification of the central optimization criterion for minimizing cortical patch size directly depends on the validity of the small-patch model. With that justification removed, the physiological meaning of the SCALE solution becomes unclear, and the rationale for favoring minimal patch size over alternative models is no longer supported.

*Examples of a large patch model*
Makeig and colleagues stated that “synchronous activity across a multi-cm cortical region has not been reported in the normal awake brain” [79]. However, there are at least two counterexamples for this statement, which exemplifies the large patch model across a multi-cm cortical region.

The first counterexample is the macroscopic traveling wave: simulation demonstrated that local coupling with neighbors supports globally extended spatiotemporal order [80,81]. Large spatial scales can be phase-organized without requiring long-range, millisecond-precise zero-lag synchrony. Synchrony is not a unitary phenomenon, and zero-lag synchrony across area is one extreme. The broad area can

be coherent but not simultaneously. There are various phase gradients and travelling waves. The traveling wave phenomena in neural field has been known since early days of scalp EEG research [82]. There is a recent surge of publications on traveling waves from high-impact journals, with the emphasis on computational modeling [83] including [84,85]. The evidence of traveling wave refutes the justification of the small patch model.

Another counterexample shows more direct evidence of large-scale, simultaneous coherence mediated by extralemniscal thalamic pathway. It has been well-demonstrated that sudden and isolated sensory stimuli (SISS) trigger some of the largest and most widespread electrocortical responses in the awake mammalian brain mediated by the extralemniscal thalamic system: for review, see [86–89]. It has some prominent characteristics including supramodality, sensitivity to inter-stimulus interval, vertex-maximum topography, and state of consciousness. In the current context, the most relevant and notable property of the extralemniscal thalamic system is that its projection is pan-cortical. The supramodality and pan-corticality was demonstrated using depth recording of mouse sensory cortex, in which auditory stimuli robustly triggered sensory cortex activation when inter-stimulus interval was 0.125 Hz [90]. Walter called non-modality-specific cortices and responses as non-specific cortex and response, respectively [87], the latter of which corresponds to responses of the extralemniscal thalamic system, and described it as follows:

> Since the fields of the evoked potentials in nonspecific areas are so widespread that no part of the head is quite unaffected by them.
>
> With this arrangement evoked responses to auditory, visual, and tactile stimuli have been recorded from the ears, chin, neck, and, in fact, all parts of the head.
>
> The most satisfactory principle is to assume that, in experiments with human subjects, all evoked responses are mainly due to nonspecific activation unless the contrary can be proved.

To provide quantitative estimates, the rate cortical neurons per thalamic neuron in the lateral geniculate nucleus is 0.1-1 % [75,91]. However, each individual axon is not restricted to a vertical column of these neurons, but spreads out tangentially and overlaps with its neighbors. As a result, this rate increases in the synaptic counts: The rate of cortex receiving thalamic input was classically estimated to be 5% in cat visual cortex [92], 6.9-8.7 % in macaque visual cortex [93]. More recent estimate using a combination of 3D-electron-microscopy and 3D-confocal imaging of thalamic boutons on macaque visual cortex, 15 and 20% for magnocellular and parvocellular pathways, respectively, which is 2 to 3 times larger than the earlier estimates. [94]. In the rodent barrel cortex, the number has been around 15 % [95–97]. These quantitative estimates suggest that extralemniscal thalamo-pancortical projection contributing to form a large-

patch cortical EEG source is anatomically plausible, refuting the explanations of the small-patch model.

*Other possible contributors to the depth bias: electrodiffusive potential*

We do not intend to attribute the observed depth bias exclusively to the large-patch mechanism. Based on our forward–inverse simulations, producing depth biases on the order of 19–26 mm would require cortical source extents of approximately 32–72 cm², which may be unusually large even under the large-patch hypothesis. This suggests that additional, underappreciated generative mechanisms may also contribute to the observed depth bias. Although a comprehensive treatment of such mechanisms lies beyond the scope of the present study, we briefly discuss one plausible contributor with important implications for future work.

One such mechanism is the soma-dendrite ionic concentration asymmetry (SDICA) current loop included in the electrodiffusive neuron-extracellular-glia (edNEG) model [98]. There is a constant imbalance of ionic concentration between dendritic and somatic layers due to differences in membrane properties. The resulting differential ion fluxes generate a constant, near-DC current loop between the layers. Although this SDICA current loop has been omitted in conventional computational models, these authors demonstrated that its contribution to local, concentration-dependent slow potentials can be of the same order of magnitude as electrodiffusive potentials [99–108]. Importantly, because SDICA-sustained current forms a dipole aligned with the somatodendritic axis of pyramidal neurons, it can contribute to scalp potential within the same volume conductor theory as conventional post-synaptic membrane currents. Although the amplitude of this contribution to scalp EEG has not been quantitatively determined, the slow time constant of the ionic concentration changes imply a wide time window for synchronization across neuronal populations. This raises the possibility that SDICA-related dipole modulations could form a spatially extended source of infraslow frequency activity below delta range, predominantly < 1 Hz. Notably, the use of relatively high cutoff frequencies for high-pass filtering (e.g., 1–2 Hz) has been reported to improve ICA performance [109]. One interpretation is that suppressing infraslow SDICA-related contributions may facilitate ICA in isolating signals predominantly derived from post-synaptic membrane potentials.

Numerical simulations of edNEG models that explicitly include SDICA remain computationally prohibitive, and realistic population-level implementations have yet to be developed. Quantifying the respective contributions of SDICA-related membrane current loops and extracellular electrodiffusive potentials to macroscopic scalp EEG therefore represents an important and largely unexplored direction for future research.

*Conclusion*

The present study showed that ICA-derived brain-class components were largely associated with physiologically implausible deep source estimates and displayed broad, depth-invariant dipole-orientation distribution. These findings contradict the small-patch model and favor the large-patch model as a more plausible physiological interpretation of ICA. A lesson from this work is that macroscopic EEG analysis requires a correct understanding of scaling laws: for example, how synchrony in as little as 1% of a neurons can outweigh the square root of total but random activity. We hope that this study motivates future investigations into whether depth bias reflects a general property of EEG source modeling and how such biases may be explained by established and emerging biophysical theories.

**Acknowledgement**

MM thanks the following researchers for insightful discussions and contributions: Edmund Wascher for information about the Dortmund dataset; Hirokazu Tanaka for discussions on the independence–dipolarity identity of ICA; Robert Oostenveld for guidance on MATLAB simulation code and foundational physiological concepts; Jorge Riera, Torbjørn Ness, and Geir Halnes for discussions on putative monopolar sources and electrodiffusive potentials; Paul Nunes for discussions on dynamic cortical source models; Giandomenico Iannetti for discussions on pan-cortical extralemniscal thalamic projections; and Scott Makeig for discussions on the small-patch model. MM also acknowledges the Linkwitz Lab by Siegfried Linkwitz for documentation on differences in spatial “illumination” between monopolar and dipolar sources, which was particularly informative.

## References


1 Comon P. Independent component analysis, A new concept? *Signal Processing* 1994;**36**:287–314. https://doi.org/10.1016/0165-1684(94)90029-9.

2 Bell AJ, Sejnowski TJ. An information-maximization approach to blind separation and blind deconvolution. *Neural Comput* 1995;**7**:1129–59. https://doi.org/10.1162/neco.1995.7.6.1129.

3 Hyvärinen A, Karhunen J, Oja E. *Independent Component Analysis*. 1st ed. New York: Wiley-Interscience; 2001.

4 Jung TP, Makeig S, Westerfield M, Townsend J, Courchesne E, Sejnowski TJ. Removal of eye activity artifacts from visual event-related potentials in normal and clinical subjects. *Clin Neurophysiol* 2000;**111**:1745–58. https://doi.org/10.1016/S1388-2457(00)00386-2.

5 Jung TP, Makeig S, Humphries C, Lee TW, McKeown MJ, Iragui V, *et al.* Removing electroencephalographic artifacts by blind source separation. *Psychophysiology* 2000;**37**:163–78. https://doi.org/10.1111/1469-8986.3720163.

6 Delorme A, Sejnowski T, Makeig S. Enhanced detection of artifacts in EEG data using higher-order statistics and independent component analysis. *Neuroimage* 2007;**34**:1443–9. https://doi.org/10.1016/j.neuroimage.2006.11.004.

7 Chaumon M, Bishop DVM, Busch NA. A practical guide to the selection of independent components of the electroencephalogram for artifact correction. *J Neurosci Methods* 2015;**250**:47–63. https://doi.org/10.1016/j.jneumeth.2015.02.025.

8 Mognon A, Jovicich J, Bruzzone L, Buiatti M. ADJUST: An automatic EEG artifact detector based on the joint use of spatial and temporal features. *Psychophysiology* 2011;**48**:229–40. https://doi.org/10.1111/j.1469-8986.2010.01061.x.

9 Winkler I, Haufe S, Tangermann M. Automatic classification of artifactual ICA-components for artifact removal in EEG signals. *Behav Brain Funct* 2011;**7**:30. https://doi.org/10.1186/1744-9081-7-30.

10 Nolan H, Whelan R, Reilly RB. FASTER: Fully Automated Statistical Thresholding for EEG artifact Rejection. *J Neurosci Methods* 2010;**192**:152–62. https://doi.org/10.1016/j.jneumeth.2010.07.015.

11 Castellanos NP, Makarov VA. Recovering EEG brain signals: artifact suppression with wavelet enhanced independent component analysis. *J Neurosci Methods* 2006;**158**:300–12. https://doi.org/10.1016/j.jneumeth.2006.05.033.

12 Jung T-P, Makeig S, McKeown MJ, Bell AJ, Lee T-W, Sejnowski TJ. Imaging Brain Dynamics Using Independent Component Analysis. *Proc IEEE Inst Electr Electron Eng* 2001;**89**:1107–22. https://doi.org/10.1109/5.939827.

13 Jung TP, Makeig S, Westerfield M, Townsend J, Courchesne E, Sejnowski TJ. Analysis and visualization of single-trial event-related potentials. *Hum Brain Mapp* 2001;**14**:166–85. https://doi.org/10.1002/hbm.1050.

14 Makeig S, Westerfield M, Jung TP, Enghoff S, Townsend J, Courchesne E, *et al.* Dynamic brain sources of visual evoked responses. *Science* 2002;**295**:690–4. https://doi.org/10.1126/science.1066168.

15 Makeig S, Debener S, Onton J, Delorme A. Mining event-related brain dynamics. *Trends Cogn Sci (Regul Ed)* 2004;**8**:204–10. https://doi.org/10.1016/j.tics.2004.03.008.

16 Makeig S, Delorme A, Westerfield M, Jung T-P, Townsend J, Courchesne E, *et al.* Electroencephalographic brain dynamics following manually responded visual targets. *PLoS Biol* 2004;**2**:e176. https://doi.org/10.1371/journal.pbio.0020176.

17 Debener S, Makeig S, Delorme A, Engel AK. What is novel in the novelty oddball paradigm? Functional significance of the novelty P3 event-related potential as revealed by independent component analysis. *Brain Res Cogn Brain Res* 2005;**22**:309–21. https://doi.org/10.1016/j.cogbrainres.2004.09.006.

18 Onton J, Delorme A, Makeig S. Frontal midline EEG dynamics during working memory. *Neuroimage* 2005;**27**:341–56. https://doi.org/10.1016/j.neuroimage.2005.04.014.

19 Onton J, Makeig S. Information-based modeling of event-related brain dynamics. *Prog Brain Res* 2006;**159**:99–120. https://doi.org/10.1016/S0079-6123(06)59007-7.

20 Onton J, Westerfield M, Townsend J, Makeig S. Imaging human EEG dynamics using independent component analysis. *Neurosci Biobehav Rev* 2006;**30**:808–22. https://doi.org/10.1016/j.neubiorev.2006.06.007.

21 Delorme A, Westerfield M, Makeig S. Medial prefrontal theta bursts precede rapid motor responses during visual selective attention. *J Neurosci* 2007;**27**:11949–59. https://doi.org/10.1523/JNEUROSCI.3477-07.2007.

22 Makeig S, Onton J. *ERP features and EEG dynamics*. Oxford University Press; 2011.

23 Delorme A, Palmer J, Onton J, Oostenveld R, Makeig S. Independent EEG sources are dipolar. *PLoS ONE* 2012;**7**:e30135. https://doi.org/10.1371/journal.pone.0030135.

24 Makeig S, Westerfield M, Townsend J, Jung TP, Courchesne E, Sejnowski TJ. Functionally independent components of early event-related potentials in a visual spatial attention task. *Philos Trans R Soc Lond B Biol Sci* 1999;**354**:1135–44. https://doi.org/10.1098/rstb.1999.0469.

25 Makeig S, Westerfield M, Jung TP, Covington J, Townsend J, Sejnowski TJ, *et al.* Functionally independent components of the late positive event-related potential during visual spatial attention. *J Neurosci* 1999;**19**:2665–80. https://doi.org/10.1523/JNEUROSCI.19-07-02665.1999.

26 Mouraux A, Iannetti GD. Nociceptive laser-evoked brain potentials do not reflect nociceptive-specific neural activity. *J Neurophysiol* 2009;**101**:3258–69. https://doi.org/10.1152/jn.91181.2008.

27 Cao C, Akalin Acar Z, Kreutz-Delgado K, Makeig S. A physiologically motivated sparse, compact, and smooth (SCS) approach to EEG source localization. *Annu Int Conf IEEE Eng Med Biol Soc* 2012;**2012**:1546–9. https://doi.org/10.1109/EMBC.2012.6346237.

28 Tsai AC, Jung T-P, Chien VSC, Savostyanov AN, Makeig S. Cortical surface alignment in multi-subject spatiotemporal independent EEG source imaging. *Neuroimage* 2014;**87**:297–310. https://doi.org/10.1016/j.neuroimage.2013.09.045.

29 Akalin Acar Z, Acar CE, Makeig S. Simultaneous head tissue conductivity and EEG source location estimation. *Neuroimage* 2016;**124**:168–80. https://doi.org/10.1016/j.neuroimage.2015.08.032.

30 Cooper R, Winter AL, Crow HJ, Walter WG. Comparison of subcortical, cortical and scalp activity using chronically indwelling electrodes in man. *Electroencephalogr Clin Neurophysiol* 1965;**18**:217–28. https://doi.org/10.1016/0013-4694(65)90088-X.

31 Ebersole JS. Defining epileptogenic foci: past, present, future. *J Clin Neurophysiol* 1997;**14**:470–83. https://doi.org/10.1097/00004691-199711000-00003.

32 Ebersole JS. Noninvasive localization of epileptogenic foci by EEG source modeling. *Epilepsia* 2000;**41 Suppl 3**:S24-33. https://doi.org/10.1111/j.1528-1157.2000.tb01531.x.

33 Cosandier-Rimélé D, Badier JM, Chauvel P, Wendling F. Modeling and interpretation of scalp-EEG and depth-EEG signals during interictal activity. *Conf Proc IEEE Eng Med Biol Soc* 2007;**2007**:4277–80. https://doi.org/10.1109/IEMBS.2007.4353281.

34 Ikeda A, Taki W, Kunieda T, Terada K, Mikuni N, Nagamine T, *et al.* Focal ictal direct current shifts in human epilepsy as studied by subdural and scalp recording. *Brain* 1999;**122 ( Pt 5)**:827–38. https://doi.org/10.1093/brain/122.5.827.

35 Hashiguchi K, Morioka T, Yoshida F, Miyagi Y, Nagata S, Sakata A, *et al.* Correlation between scalp-recorded electroencephalographic and electrocorticographic activities during ictal period. *Seizure* 2007;**16**:238–47. https://doi.org/10.1016/j.seizure.2006.12.010.

36 Kobayashi K, Yoshinaga H, Ohtsuka Y, Gotman J. Dipole modeling of epileptic spikes can be accurate or misleading. *Epilepsia* 2005;**46**:397–408. https://doi.org/10.1111/j.0013-9580.2005.31404.x.

37 Nunez PL, Srinivasan R. *Electric fields of the brain*. 198 Madison Avenue, New York, New York, 10016: Oxford University Press, Inc; 2006.

38 Tao JX, Ray A, Hawes-Ebersole S, Ebersole JS. Intracranial EEG substrates of scalp EEG interictal spikes. *Epilepsia* 2005;**46**:669–76. https://doi.org/10.1111/j.1528-1167.2005.11404.x.

39 Tao JX, Baldwin M, Ray A, Hawes-Ebersole S, Ebersole JS. The impact of cerebral source area and synchrony on recording scalp electroencephalography ictal patterns. *Epilepsia* 2007;**48**:2167–76. https://doi.org/10.1111/j.1528-1167.2007.01224.x.

40 Díaz-Caneja CM, Alloza C, Gordaliza PM, Fernández-Pena A, de Hoyos L, Santonja J, *et al.* Sex differences in lifespan trajectories and variability of human sulcal and gyral morphology. *Cereb Cortex* 2021;**31**:5107–20. https://doi.org/10.1093/cercor/bhab145.

41 Van Essen DC, Drury HA. Structural and functional analyses of human cerebral cortex using a surface-based atlas. *J Neurosci* 1997;**17**:7079–102. https://doi.org/10.1523/JNEUROSCI.17-18-07079.1997.

42 Zilles K, Armstrong E, Schleicher A, Kretschmann HJ. The human pattern of gyrification in the cerebral cortex. *Anat Embryol* 1988;**179**:173–9. https://doi.org/10.1007/BF00304699.

43 Stark AK, Toft MH, Pakkenberg H, Fabricius K, Eriksen N, Pelvig DP, *et al.* The effect of age and gender on the volume and size distribution of neocortical

neurons. *Neuroscience* 2007;**150**:121–30. https://doi.org/10.1016/j.neuroscience.2007.06.062.

44 Pakkenberg B, Gundersen HJ. Neocortical neuron number in humans: effect of sex and age. *J Comp Neurol* 1997;**384**:312–20. https://doi.org/10.1002/(SICI)1096-9861(19970728)384:2<312::AID-CNE10>3.0.CO;2-K.

45 Acar ZA, Makeig S. Neuroelectromagnetic forward head modeling toolbox. *J Neurosci Methods* 2010;**190**:258–70. https://doi.org/10.1016/j.jneumeth.2010.04.031.

46 Oostenveld R, Fries P, Maris E, Schoffelen J-M. FieldTrip: Open source software for advanced analysis of MEG, EEG, and invasive electrophysiological data. *Comput Intell Neurosci* 2011;**2011**:156869. https://doi.org/10.1155/2011/156869.

47 Næss S, Chintaluri C, Ness TV, Dale AM, Einevoll GT, Wójcik DK. Corrected Four-Sphere Head Model for EEG Signals. *Front Hum Neurosci* 2017;**11**:490. https://doi.org/10.3389/fnhum.2017.00490.

48 Babayan A, Erbey M, Kumral D, Reinelt JD, Reiter AMF, Röbbig J, *et al.* A mind-brain-body dataset of MRI, EEG, cognition, emotion, and peripheral physiology in young and old adults. *Sci Data* 2019;**6**:180308. https://doi.org/10.1038/sdata.2018.308.

49 Getzmann S, Gajewski PD, Schneider D, Wascher E. Resting-state EEG data before and after cognitive activity across the adult lifespan and a 5-year follow-up. *Sci Data* 2024;**11**:988. https://doi.org/10.1038/s41597-024-03797-w.

50 Oostenveld R, Praamstra P. The five percent electrode system for high-resolution EEG and ERP measurements. *Clin Neurophysiol* 2001;**112**:713–9. https://doi.org/10.1016/S1388-2457(00)00527-7.

51 Kim H, Luo J, Chu S, Cannard C, Hoffmann S, Miyakoshi M. ICA's bug: How ghost ICs emerge from effective rank deficiency caused by EEG electrode interpolation and incorrect re-referencing. *Front Signal Process* 2023;**3**:. https://doi.org/10.3389/frsip.2023.1064138.

52 Delorme A, Makeig S. EEGLAB: an open source toolbox for analysis of single-trial EEG dynamics including independent component analysis. *J Neurosci Methods* 2004;**134**:9–21. https://doi.org/10.1016/j.jneumeth.2003.10.009.

53 Collins DL, Neelin P, Peters TM, Evans AC. Automatic 3D intersubject registration of MR volumetric data in standardized Talairach space. *J Comput Assist Tomogr* 1994;**18**:192–205. https://doi.org/10.1097/00004728-199403000-00005.

54 Evans AC, Collins DL, Mills SR, Brown ED, Kelly RL, Peters TM. 3D Statistical Neuroanatomical Models from 305 MRI Volumes. Presented at the 1993 IEEE Conference Record Nuclear Science Symposium and Medical Imaging Conference.

55 Kothe C, Jung T-P. Artifact removal techniques with signal reconstruction. US20160113587A1, 2016.

56 Kothe CA, Makeig S. BCILAB: a platform for brain-computer interface development. *J Neural Eng* 2013;**10**:056014. https://doi.org/10.1088/1741-2560/10/5/056014.

57 Chang C-Y, Hsu S-H, Pion-Tonachini L, Jung T-P. Evaluation of artifact subspace reconstruction for automatic EEG artifact removal. *Annu Int Conf IEEE Eng Med Biol Soc* 2018;**2018**:1242–5. https://doi.org/10.1109/EMBC.2018.8512547.

58 Chang C-Y, Hsu S-H, Pion-Tonachini L, Jung T-P. Evaluation of Artifact Subspace Reconstruction for Automatic Artifact Components Removal in Multi-Channel EEG Recordings. *IEEE Trans Biomed Eng* 2020;**67**:1114–21. https://doi.org/10.1109/TBME.2019.2930186.

59 Anders P, Müller H, Skjæret-Maroni N, Vereijken B, Baumeister J. The influence of motor tasks and cut-off parameter selection on artifact subspace reconstruction in EEG recordings. *Med Biol Eng Comput* 2020;**58**:2673–83. https://doi.org/10.1007/s11517-020-02252-3.

60 Miyakoshi M. Artifact subspace reconstruction (ASR): A candidate for a dream solution for EEG studies, sleep or awake. *Sleep* 2023:zsad241. https://doi.org/10.1093/sleep/zsad241.

61 Kim H, Chang C-Y, Kothe C, Iversen JR, Miyakoshi M. Juggler's ASR: Unpacking the principles of artifact subspace reconstruction for revision toward extreme MoBI. *J Neurosci Methods* 2025;**420**:110465. https://doi.org/10.1016/j.jneumeth.2025.110465.

62 Palmer J, Kreutz-delgado K, Makeig S. AMICA: An Adaptive Mixture of Independent Component Analyzers with Shared Components 2016.

63 Pion-Tonachini L, Kreutz-Delgado K, Makeig S. ICLabel: An automated electroencephalographic independent component classifier, dataset, and website. *Neuroimage* 2019;**198**:181–97. https://doi.org/10.1016/j.neuroimage.2019.05.026.

64 Piazza C, Miyakoshi M, Akalin-Acar Z, Cantiani C, Reni G, Bianchi AM, *et al.* An Automated Function for Identifying EEG Independent Components Representing

Bilateral Source Activity. In: Kyriacou E, Christofides S, Pattichis CS, editors. *XIV Mediterranean Conference on Medical and Biological Engineering and Computing 2016*, vol. 57. Cham: Springer International Publishing; 2016. p. 105–9.

65 Mazziotta JC, Toga AW, Evans A, Fox P, Lancaster J. A probabilistic atlas of the human brain: theory and rationale for its development. The International Consortium for Brain Mapping (ICBM). *Neuroimage* 1995;**2**:89–101. https://doi.org/10.1006/nimg.1995.1012.

66 Fonov VS, Evans AC, Botteron K, Almli CR, McKinstry RC, Collins DL, *et al.* Unbiased average age-appropriate atlases for pediatric studies. *Neuroimage* 2011;**54**:313–27. https://doi.org/10.1016/j.neuroimage.2010.07.033.

67 Tzourio-Mazoyer N, Landeau B, Papathanassiou D, Crivello F, Etard O, Delcroix N, *et al.* Automated anatomical labeling of activations in SPM using a macroscopic anatomical parcellation of the MNI MRI single-subject brain. *Neuroimage* 2002;**15**:273–89. https://doi.org/10.1006/nimg.2001.0978.

68 Donoghue T, Haller M, Peterson EJ, Varma P, Sebastian P, Gao R, *et al.* Parameterizing neural power spectra into periodic and aperiodic components. *Nat Neurosci* 2020;**23**:1655–65. https://doi.org/10.1038/s41593-020-00744-x.

69 Budd JM, Kisvárday ZF. Local lateral connectivity of inhibitory clutch cells in layer 4 of cat visual cortex (area 17). *Exp Brain Res* 2001;**140**:245–50. https://doi.org/10.1007/s002210100817.

70 Stettler DD, Das A, Bennett J, Gilbert CD. Lateral connectivity and contextual interactions in macaque primary visual cortex. *Neuron* 2002;**36**:739–50. https://doi.org/10.1016/s0896-6273(02)01029-2.

71 Stepanyants A, Martinez LM, Ferecskó AS, Kisvárday ZF. The fractions of short- and long-range connections in the visual cortex. *Proc Natl Acad Sci USA* 2009;**106**:3555–60. https://doi.org/10.1073/pnas.0810390106.

72 Hari R, Salmelin R, Mäkelä JP, Salenius S, Helle M. Magnetoencephalographic cortical rhythms. *Int J Psychophysiol* 1997;**26**:51–62. https://doi.org/10.1016/S0167-8760(97)00755-1.

73 Hari R. The neuromagnetic method in the study of the human auditory cortex. *Advances in Audiology* 1990;**6**:222–82.

74 Kanari L, Ramaswamy S, Shi Y, Morand S, Meystre J, Perin R, *et al.* Objective morphological classification of neocortical pyramidal cells. *Cereb Cortex* 2019;**29**:1719–35. https://doi.org/10.1093/cercor/bhy339.

75 O'Kusky J, Colonnier M. A laminar analysis of the number of neurons, glia, and synapses in the adult cortex (area 17) of adult macaque monkeys. *J Comp Neurol* 1982;**210**:278–90. https://doi.org/10.1002/cne.902100307.

76 Elul R. The genesis of the EEG. *Int Rev Neurobiol* 1971;**15**:227–72. https://doi.org/10.1016/S0074-7742(08)60333-5.

77 Walter WG, Cooper R, Aldridge VJ, Mccallum WC, Winter AL. Contingent negative variation: an electric sign of sensorimotor association and expectancy in the human brain. *Nature* 1964;**203**:380–4.

78 Deco G, Jirsa VK, Robinson PA, Breakspear M, Friston K. The dynamic brain: from spiking neurons to neural masses and cortical fields. *PLoS Comput Biol* 2008;**4**:e1000092. https://doi.org/10.1371/journal.pcbi.1000092.

79 Whitmer D, Worrell G, Stead M, Lee IK, Makeig S. Utility of independent component analysis for interpretation of intracranial EEG. *Front Hum Neurosci* 2010;**4**:184. https://doi.org/10.3389/fnhum.2010.00184.

80 Jeong S-O, Ko T-W, Moon H-T. Time-delayed spatial patterns in a two-dimensional array of coupled oscillators. *Phys Rev Lett* 2002;**89**:154104. https://doi.org/10.1103/PhysRevLett.89.154104.

81 Udeigwe LC, Ermentrout GB. Waves and patterns on regular graphs. *SIAM J Appl Dyn Syst* 2015;**14**:1102–29. https://doi.org/10.1137/140969488.

82 Hughes JR. The phenomenon of travelling waves: a review. *Clin Electroencephalogr* 1995;**26**:1–6.

83 Dugué L, Chavane F. Traveling waves across scales: Different mechanisms but same canonical computation? *ELife* 2025;**14**:. https://doi.org/10.7554/eLife.106753.

84 Muller L, Chavane F, Reynolds J, Sejnowski TJ. Cortical travelling waves: mechanisms and computational principles. *Nat Rev Neurosci* 2018;**19**:255–68. https://doi.org/10.1038/nrn.2018.20.

85 Halgren M, Ulbert I, Bastuji H, Fabó D, Erőss L, Rey M, *et al.* The generation and propagation of the human alpha rhythm. *Proc Natl Acad Sci USA* 2019;**116**:23772–82. https://doi.org/10.1073/pnas.1913092116.

86 Albe-Fessard D, Besson JM. Convergent Thalamic and Cortical Projections — The Non-Specific System. In: Iggo A, editor. *Somatosensory System*, vol. 2. Berlin, Heidelberg: Springer Berlin Heidelberg; 1973. p. 489–560.

87 Walter WG. The convergence and interaction of visual, auditory, and tactile responses in human nonspecific cortex. *Ann N Y Acad Sci* 1964;**112**:320–61. https://doi.org/10.1111/j.1749-6632.1964.tb26760.x.

88 Somervail R, Perovic S, Bufacchi RJ, Caminiti R, Iannetti GD. A two-system theory of sensory-evoked brain responses. *Brain* 2025. https://doi.org/10.1093/brain/awaf402.

89 Miyakoshi M, Kim H, De Stefano LA, Schmitt LM, Norris JE, Ethridge LE, *et al.* Hyper-extralemniscal model of Fragile X syndrome. *Cereb Cortex* 2025;**35**:. https://doi.org/10.1093/cercor/bhaf141.

90 Benusiglio D, Asari H. Sudden sensory events trigger modality-independent responses across layers in the mouse neocortex. *BioRxiv* 2024. https://doi.org/10.1101/2024.11.07.622472.

91 Connolly M, Van Essen D. The representation of the visual field in parvicellular and magnocellular layers of the lateral geniculate nucleus in the macaque monkey. *J Comp Neurol* 1984;**226**:544–64. https://doi.org/10.1002/cne.902260408.

92 Peters A, Payne BR. Numerical relationships between geniculocortical afferents and pyramidal cell modules in cat primary visual cortex. *Cereb Cortex* 1993;**3**:69–78. https://doi.org/10.1093/cercor/3.1.69.

93 Latawiec D, Martin KA, Meskenaite V. Termination of the geniculocortical projection in the striate cortex of macaque monkey: a quantitative immunoelectron microscopic study. *J Comp Neurol* 2000;**419**:306–19. https://doi.org/10.1002/(sici)1096-9861(20000410)419:3<306::aid-cne4>3.0.co;2-2.

94 Garcia-Marin V, Kelly JG, Hawken MJ. Major feedforward thalamic input into layer 4C of primary visual cortex in primate. *Cereb Cortex* 2019;**29**:134–49. https://doi.org/10.1093/cercor/bhx311.

95 Benshalom G, White EL. Quantification of thalamocortical synapses with spiny stellate neurons in layer IV of mouse somatosensory cortex. *J Comp Neurol* 1986;**253**:303–14. https://doi.org/10.1002/cne.902530303.

96 Bruno RM, Sakmann B. Cortex is driven by weak but synchronously active thalamocortical synapses. *Science* 2006;**312**:1622–7. https://doi.org/10.1126/science.1124593.

97 Schoonover CE, Tapia J-C, Schilling VC, Wimmer V, Blazeski R, Zhang W, *et al.* Comparative strength and dendritic organization of thalamocortical and

corticocortical synapses onto excitatory layer 4 neurons. *J Neurosci* 2014;**34**:6746–58. https://doi.org/10.1523/JNEUROSCI.0305-14.2014.

98 Sætra MJ, Einevoll GT, Halnes G. An electrodiffusive neuron-extracellular-glia model for exploring the genesis of slow potentials in the brain. *PLoS Comput Biol* 2021;**17**:e1008143. https://doi.org/10.1371/journal.pcbi.1008143.

99 Halnes G, Ostby I, Pettersen KH, Omholt SW, Einevoll GT. Electrodiffusive model for astrocytic and neuronal ion concentration dynamics. *PLoS Comput Biol* 2013;**9**:e1003386. https://doi.org/10.1371/journal.pcbi.1003386.

100 Halnes G, Østby I, Pettersen KH, Omholt SW, Einevoll GT. An electrodiffusive formalism for ion concentration dynamics in excitable cells and the extracellular space surrounding them. In: Liljenström H, editor. *Advances in cognitive neurodynamics (IV)*. Dordrecht: Springer Netherlands; 2015. p. 353–60.

101 Halnes G, Mäki-Marttunen T, Keller D, Pettersen KH, Andreassen OA, Einevoll GT. Effect of ionic diffusion on extracellular potentials in neural tissue. *PLoS Comput Biol* 2016;**12**:e1005193. https://doi.org/10.1371/journal.pcbi.1005193.

102 Halnes G, Mäki-Marttunen T, Pettersen KH, Andreassen OA, Einevoll GT. Ion diffusion may introduce spurious current sources in current-source density (CSD) analysis. *J Neurophysiol* 2017;**118**:114–20. https://doi.org/10.1152/jn.00976.2016.

103 Solbrå A, Bergersen AW, van den Brink J, Malthe-Sørenssen A, Einevoll GT, Halnes G. A Kirchhoff-Nernst-Planck framework for modeling large scale extracellular electrodiffusion surrounding morphologically detailed neurons. *PLoS Comput Biol* 2018;**14**:e1006510. https://doi.org/10.1371/journal.pcbi.1006510.

104 Ness TV, Halnes G, Næss S, Pettersen KH, Einevoll GT. Computing Extracellular Electric Potentials from Neuronal Simulations. *Adv Exp Med Biol* 2022;**1359**:179–99. https://doi.org/10.1007/978-3-030-89439-9_8.

105 Halnes G, Ness TV, Næss S, Hagen E, Pettersen KH, Einevoll GT. Diffusion potentials in brain tissue. *Electric brain signals: foundations and applications of biophysical modeling*. Cambridge University Press; 2024. p. 289–308.

106 Qian N, Sejnowski TJ. An electro-diffusion model for computing membrane potentials and ionic concentrations in branching dendrites, spines and axons. *Biol Cybern* 1989;**62**:1–15. https://doi.org/10.1007/BF00217656.

107 Savtchenko LP, Poo MM, Rusakov DA. Electrodiffusion phenomena in neuroscience: a neglected companion. *Nat Rev Neurosci* 2017;**18**:598–612. https://doi.org/10.1038/nrn.2017.101.

108 Sætra MJ, Einevoll GT, Halnes G. An electrodiffusive, ion conserving Pinsky-Rinzel model with homeostatic mechanisms. *PLoS Comput Biol* 2020;**16**:e1007661. https://doi.org/10.1371/journal.pcbi.1007661.

109 Winkler I, Debener S, Müller K-R, Tangermann M. On the influence of high-pass filtering on ICA-based artifact reduction in EEG-ERP. *Conf Proc IEEE Eng Med Biol Soc* 2015;**2015**:4101–5. https://doi.org/10.1109/EMBC.2015.7319296.